Chemical Engineering Journal 485 (2024) 149587

Contents lists available at ScienceDirect

Chemical Engineering Journal

journal homepage: www.elsevier.com/locate/cej

Fine-tuning the pore environment of isoreticular metal-organic frameworks through installing functional sites for boosting C_2H_6/C_2H_4 separation

Gang-Ding Wang [a], Yong-Zhi Li [c,*], Rajamani Krishna [b], Zhi-Zhu Yan [a], Lei Hou [a,*], Yao-Yu Wang [a], Zhonghua Zhu [d]

[a] Key Laboratory of Synthetic and Natural Functional Molecule of the Ministry of Education, Shaanxi Key Laboratory of Physico-Inorganic Chemistry, College of Chemistry & Materials Science, Northwest University, Xi'an 710069, PR China
[b] Van 't Hoff Institute for Molecular Sciences University of Amsterdam Science Park 904, 1098 XH Amsterdam, The Netherlands
[c] School of Materials and Physics, China University of Mining and Technology, Xuzhou 221116, PR China
[d] School of Chemical Engineering, The University of Queensland, Brisbane 4072, Australia

ARTICLE INFO

Keywords:
Metal-organic framework
C_2H_6-selective MOFs
Reticular chemistry
Pore engineering
C_2H_6/C_2H_4 separation

ABSTRACT

Herein, we presented a strategy that tuning the pore environment *via* installing functional sites in the pores to boost C_2H_6/C_2H_4 separation performance of MOFs. To prove this strategy, four isoreticular MOFs [MAF-X10, -X10(Me), -X10(Cl), and -X10(F)] were designed and synthesized based on reticular chemistry principle, which featured the regulated pore environment and exhibited intriguing differences in C_2H_6 and C_2H_4 uptakes. Methyl group-modified nonpolar pores endow these MOFs with impressive C_2H_6-selective behavior and high C_2H_6 loadings (>110 $cm^3\ g^{-1}$), in which MAF-X10(F) with polar F sites exhibited the highest C_2H_6 uptake (140.5 $cm^3\ g^{-1}$) among four MOFs, ranking the top compared to the reported MOF materials. The polar sites-functionalized MAF-X10(Cl) and -X10(F) showed the significantly improved C_2H_6/C_2H_4 separation performances in comprehensive of selectivity, separation potential, C_2H_4 productivity, which were mainly contributed to the strong C-H···Cl/F interactions formed between the active sites (Cl or F) in MAF-X10(Cl)/(F) and C_2H_6, as revealed by molecular simulations.

1. Introduction

Ethylene (C_2H_4) as the major chemical feedstock in industrial production is generally produced *via* thermal decomposition or steam cracking of either ethane (C_2H_6) or naphtha, where approximately 35 % or 4 % C_2H_6 impurities inevitably coexist as byproducts in the cracking of C_2H_6 or naphtha process, respectively [1–5]. Thus, C_2H_6/C_2H_4 separation process is the crux of C_2H_4 polymerization industry since polymer grade C_2H_4 is needed for downstream synthesis [6,7]. This separation is typically dependent on the cryogenic distillation under high pressures due to very similar physicochemical properties between C_2H_4 and C_2H_6 (Scheme S1), wherein the energy consumption is very giant [8,9]. So the development of alternative separation processes is highly sought after, yet largely unexplored. Recently, physisorptive separation based on porous adsorbents that combining high selectivity, easy operation, and low energy consumption has been proposed as highly efficient approach [10–12].

Metal-organic frameworks (MOFs) with high porosity, controllable pore size, and regulated pore environment have been developed as promising candidates for addressing the challenging separation [13–22]. For C_2H_4/C_2H_6 separation, the C_2H_6-selective MOF which preferentially adsorbed C_2H_6 impurity over C_2H_4 achieved very efficient process of producing high-purity C_2H_4 in one step [23–25]. Although some C_2H_6-selective MOFs based on various mechanisms including hydrogen bonds, multiple C-H···π interactions, and gate-opening effect have been constructed, they still usually suffer from "trade-off" effect with either low adsorption capacity because of small pore volumes or low selectivity owing to lacking special recognition sites. For instance, flexible ZIF-7 [26] could preferentially adsorb C_2H_6 over C_2H_4 based on gate-opening mechanism, however, displayed low C_2H_4 productivity owing to close gate-opening pressures of two gases. MAF-49 [27] and Cu $(Qc)_2$ [28] showed the high C_2H_6/C_2H_4 selectivity (2.7 and 3.4), but both possessed the low C_2H_6 loadings (38.0 and 41.4 $cm^3\ g^{-1}$) due to small cavities. Notably, the material $Fe_2(O_2)$(dobdc) obtained through modifying iron sites with O_2 achieved high C_2H_6 uptake and significant C_2H_6/C_2H_4 selectivity [29], whereas the material needed to be operated

* Corresponding authors.
E-mail addresses: Lyz2021@cumt.edu.cn (Y.-Z. Li), lhou2009@nwu.edu.cn (L. Hou).

https://doi.org/10.1016/j.cej.2024.149587
Received 20 December 2023; Received in revised form 8 February 2024; Accepted 11 February 2024
Available online 13 February 2024

in a glove box under inert conditions, causing a critical restriction for applications.

One constant challenge in designing MOF adsorbents is the existence of almost inevitable "trade-off" effect between high selectivity and high capacity. So the design of rational pore environments that directly decide the adsorption capacity of MOFs for different gases is very crucial to solve this dilemma. The regulation of pore through bottom-up pore engineering strategy provides an important approach to create suitable pore environments that facilitate the preferential adsorption of MOFs for target gas. Reticular chemistry that was proposed by Yaghi has recently become an important tool in crystal design [30], which can enable us to accurately control and design pore environment and function of frameworks to obtain outstanding materials for separation tasks. Unfortunately, there are currently very few direct experiments to systematically study the C_2H_6/C_2H_4 separation through precise pore tuning [28,31,32].

In latest study, we evidenced that the nonpolar pore surfaces are advantageous to create the C_2H_6-selective MOFs for C_2H_6/C_2H_4 separation [33,34]. However, to decrease the "trade-off" effect in adsorption, the creation of additional binding sites toward C_2H_6 are crucial for MOF design. Fluorine (F) atom with low polarizability and high electronegativity is an excellent acceptor to form hydrogen bonds. Meanwhile, F substitution in MOFs could impactfully change the physico-chemical properties of MOFs since the radical difference of polarizability and electronegativity between F and H atoms. Thus, F-functionalization is an effective approach to enhance the gas storage and separation performance in MOFs [32,35,36]. We speculated that the installation of polar sites (F or Cl atoms) in nonpolar/inert pore environment of framework with large pore volume is of great importance to obtain excellent C_2H_6/C_2H_4 separation performance of MOFs, as illustrated in Scheme 1.

During the continuous effort to seek exceptional C_2H_6/C_2H_4 separation materials, a highly porous framework $[Zn_4O(bpz)_2(bdc)]$ (namely MAF-X10) reported by us was herein screened out [37]. MAF-X10 based on the $[Zn_4O]^{6+}$ cores and mixed 1,4-benzenedicarboxylatic acid (H_2bdc) and 3,3′,5,5′-tetramethyl-4,4′-bipyrazole (H_2bpz) linkers contains rich methyl groups in pore wall, providing nonpolar environment for preferential adsorption of C_2H_6 over C_2H_4. Through taking the strategy of ligand decoration, isomorphic MAF-X10(Me), MAF-X10(Cl), and MAF-X10(F) with finely-tuned pore environments were designed by functionalized dicarboxylates: H_2bdc-Me, H_2bdc-Cl, and H_2bdc-F, which as C_2H_6-selective materials provided a new platform for comparative investigation of C_2H_6/C_2H_4 separation. The stronger interactions between the polar adsorption sites (Cl or F) of MAF-X10(Cl)/(F) and C_2H_6 was evidenced by molecular simulations. The C_2H_6 adsorption amounts deferred to the order of MAF-X10(F) > MAF-X10(Cl) > MAF-X10(Me) ≈ MAF-X10. Remarkably, MAF-X10(F) displays the second highest C_2H_6 uptake (200.7 $cm^3\ g^{-1}$ at 273 K under 100 kPa) among the known C_2H_6-selective MOFs as well as the optimized adsorption selectivity and dynamic separation for C_2H_6/C_2H_4 mixtures.

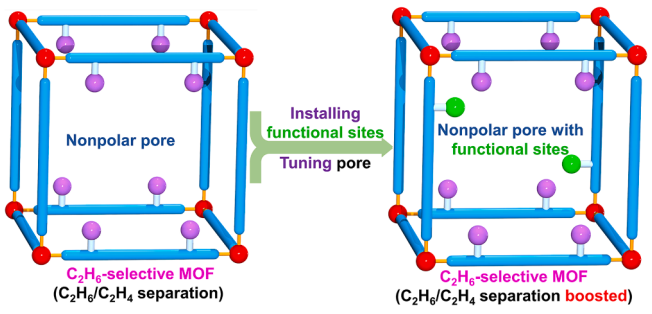

Scheme 1. Schematic illustration of tuning pore of MOFs to enhance C_2H_6/C_2H_4 separation.

2. Experimental

2.1. Materials and general methods

These contents were provided in Supporting Information.

2.2. Synthesis of $[Zn_4O(bpz)_2(bdc)]\cdot 4H_2O\cdot 4DMF$ MAF-X10

The MAF-X10 was synthesized according to reported literature procedure with slight modification [37]. In a typical process, $Zn(NO_3)_2\cdot 6H_2O$ (0.179 g), 1,4-benzenedicarboxylic acid (H_2bdc) (0.021 g), 3,3′,5,5′-tetramethyl-4,4′bipyrazole (H_2bpz) (0.057 g), N,N-dimethylformamide (DMF) (9 mL) were placed in a 15 mL Teflon-lined reactor. The mixture was heated at 140 °C for 72 h and slowly cooled to room temperature. Colorless block crystals of MAF-X10 were collected. Anal. Calcd for $C_{40}H_{64}N_{12}O_{13}Zn_4$: C, 40.62; H, 5.45; N, 14.21%. Found: C, 40.50; H, 5.51; N, 14.32%.

2.3. Synthesis $[Zn_4O(bpz)_2(bdc\text{-}Me)]\cdot 4H_2O\cdot 4DMF$ MAF-X10(Me)

Single crystals for X-ray single-crystal diffraction were prepared by heating a solution of 2-methyl-1,4-benzenedicarboxylic acid (H_2bdc-Me) (0.008 g), H_2bpz (0.014 g), and $Zn(NO_3)_2\cdot 6H_2O$ (0.045 g) in a mixed solvent of DMF (3 mL), methanol (2 mL) in a 15 mL Teflon-lined stainless steel vessel at 140 °C for 72 h, then the mixture was cooled to room temperature at a rate of 5 °C h^{-1} to give colorless block single crystals. Anal. Calcd for $C_{41}H_{66}N_{12}O_{13}Zn_4$: C, 41.15; H, 5.56; N, 14.04%. Found: C, 41.27; H, 5.70; N, 14.16%.

2.4. Synthesis of $[Zn_4O(bpz)_2(bdc\text{-}F)]\cdot 2H_2O\cdot 2DMF$ MAF-X10(F)

Single crystals for X-ray single-crystal diffraction were prepared by heating a solution of 2-fluoro-1,4-benzenedicarboxylic acid (H_2bdc-F) (0.008 g), H_2bpz (0.014 g), and $Zn(NO_3)_2\cdot 6H_2O$ (0.045 g) in a mixed solvent of DMF (3 mL), methanol (2 mL) in a 15 mL Teflon-lined stainless steel vessel at 140 °C for 72 h, then the mixture was cooled to room temperature at a rate of 5 °C h^{-1} to give colorless block single crystals. Anal. Calcd for $C_{34}H_{45}FN_{10}O_9Zn_4$: C, 40.09; H, 4.45; N, 13.75%. Found: C, 39.89; H, 4.52; N, 13.61%.

2.5. Synthesis of $[Zn_4O(bpz)_2(bdc\text{-}Cl)]\cdot 2H_2O\cdot 2DMF$ MAF-X10(Cl)

Single crystals for X-ray single-crystal diffraction were prepared by heating a solution of 2-chloro-1,4-benzenedicarboxylic acid (H_2bdc-Cl) (0.008 g), H_2bpz (0.014 g), and $Zn(NO_3)_2\cdot 6H_2O$ (0.045 g) in a mixed solvent of DMF (3 mL), methanol (2 mL) in a 15 mL Teflon-lined stainless steel vessel at 140 °C for 72 h, then the mixture was cooled to room temperature at a rate of 5 °C h^{-1} to give colorless block single crystals. Anal. Calcd for $C_{34}H_{45}ClN_{10}O_9Zn_4$: C, 39.46; H, 4.38; N, 13.53 %. Found: C, 39.31; H, 4.50; N, 13.41 %.

3. Results and discussion

3.1. Pore engineering

Considering that C_2H_4 has a smaller polarizability and larger quadrupole moment than C_2H_6, we elaborately selected MAF-X10 that had high porosity and rich hydrophobic methyl groups in pores as a platform for functionalization to target C_2H_6/C_2H_4 separation. Referring to the synthesis of MAF-X10, the solvothermal reaction of $Zn(NO_3)_2$, H_2bpz, and H_2bdc with different substituent groups of -Me, -Cl or -F yielded three new MOFs, namely MAF-X10(Me), MAF-X10(Cl), and MAF-X10(F), respectively. Single-crystal structure indicated that the nets of MAF-X10(Me), -X10(Cl), and -X10(F) are isostructural to MAF-X10 with 6-connected pcu topology, which are composed of octahedral $Zn_4O(CO_2)_2(NN)_4$ SBUs, and linearly-connected bdc and bpz linkers to build a

3D framework. The zinc centers are fully covered by the methyl groups and thus no accessible open metal sites (OMSs). The solvent accessible volumes of MAF-X10, -X10(Me), -X10(Cl), and -X10(F) were estimated by PLATON to be 63.3 %, 59.8 %, 57.5 %, and 59.0 %, respectively. For the four frameworks, the pore sizes along the *c* axis are almost the same of 5.7 × 5.7 $Å^2$, however, the apertures sizes for MAF-X10, MAF-X10 (Me), -X10(Cl), and -X10(F) are determined to be 4.9 × 6.8, 4.9 × 5.8, 4.9 × 6.2, and 4.9 × 6.5 $Å^2$, respectively, along the *a* axis or *b* axis due to different substituent groups in H_2bdc (Fig. 1). So the surface components of four MOFs are exactly regulated, which is desired for us to precisely investigate the regulation of substituent group changes on optimizing C_2H_6/C_2H_4 separation performance.

3.2. Characterization

The consistency of the powder X-ray diffraction (PXRD) between as-synthesized samples and simulated results confirmed the phase purity and crystallinity of MAF-X10 isomorphs (Fig. S1). Thermogravimetric analysis (TGA) results revealed the release of guest molecules at about 120–150 °C for MAF-X10 isomorphs, and then no further weight loss before 400 °C (Fig. S2). The frameworks can be entirely activated by heating the dichloromethane-exchanged samples at 120 °C under vacuum (4 h), as confirmed by TGA.

3.3. Adsorption amount

Nitrogen (N_2) adsorption experiments at 77 K showed similar type-I adsorption curves for the four MOFs, registering the saturated loadings of 433, 476, 460, and 507 $cm^3\ g^{-1}$ for MAF-X10, -X10(Me), -X10(Cl), and -X10(F), respectively, indicating high microporosity (Fig. 2a). The corresponding Brunauer-Emmett-Teller (BET) surface areas were calculated to be 1644, 1782, 1751, and 1931 $m^2\ g^{-1}$, and the accessible pore volume were 0.67, 0.62, 0.63, and 0.67 $cm^3\ g^{-1}$, respectively, agreeing with the values of 0.7–0.8 $cm^3\ g^{-1}$ calculated from crystal data. The accessible pore surfaces of these MOFs are mainly modified by methyl groups and aromatic rings, resulting in a hydrophobic pore environment. We then measured the water vapor adsorption isotherms of these MOFs at 298 K (Fig. S3) displayed type-V isotherms with the starting point of major water uptake region located at about P/P_0 = 0.5–0.7, indicated the relatively strong pore hydrophobicity and also agreed with the nonpolar features of pores [38–40], which would be favorable for C_2H_6/C_2H_4 separation. In addition, these MOFs maintained the framework crystallinity and integrity after the water adsorption, as demonstrated by PXRD results in Fig. S1. The stability can be attributed to the hiding of Zn^{2+} ions by the methyl groups in ligands, which prevented the water molecules from attacking on the metal centres.

The nonpolar pore walls with different accessible substituent sites in present MOF platforms prompted us to measure C_2H_6 and C_2H_4 adsorption for evaluating the C_2H_6/C_2H_4 separation performance. As provided in Fig. 2b-2e, at 273/298 K under 100 kPa, the adsorption amounts of MAF-X10, -X10(Me), -X10(Cl), and -X10(F) for C_2H_4 were 132.1/80.0, 139.0/89.9, 151.7/90.7, and 146/91.7 $cm^3\ g^{-1}$, respectively, and which were increased to 172.9/113.6, 165.9/112.2, 186.9/131.5, and 200.7/140.5 $cm^3\ g^{-1}$ for C_2H_6, respectively. There were more significantly high for the uptakes from C_2H_4 to C_2H_6 in MAF-X10 (Cl) (44.9 %) and -X10(F) (53.2 %) compared to MAF-X10 (42.0 %) and -X10(Me) (24.8 %), namely, the F and Cl groups in the pores increased the C_2H_6 uptakes in a larger degree. Notably, for MAF-X10(F), the C_2H_6 uptake at 298 K is the fifth highest among all reported C_2H_6-selective MOFs, which is only lower than SNNU-40 (169 $cm^3\ g^{-1}$) [41], CPM-233 (166 $cm^3\ g^{-1}$) [42], CPM-733 (159.6 $cm^3\ g^{-1}$) [42], and Ni-1a (147.8 $cm^3\ g^{-1}$) [43]; especially, the C_2H_6 uptake of MAF-X10(F) at 273 K ranks top two, only inferior to SNNU-40 (289 $cm^3\ g^{-1}$) (Fig. 2f) [41]. It is apparent that the loadings for C_2H_4 were lower than C_2H_6 for MAF-X10 isomorphs in measured full pressure region, indicating selective adsorption of C_2H_6 over C_2H_4. Meanwhile, the adsorption enthalpy (Q_{st}) which was calculated by fitting adsorption isotherms at 273 and 298 K using the 1-site Langmuir-Freundlich model also revealed the obviously higher initial Q_{st} values for C_2H_6 (23.4–26.7 kJ mol^{-1}) relative to C_2H_4 (21.2–23.5 kJ mol^{-1}) (Fig. S4, Tables S1–S4). It is worth noting that the Q_{st} values of C_2H_6 and C_2H_4 for the four MOFs are moderate (<30 kJ mol^{-1}), implying a facile regeneration treatment and low regeneration energy. In fact, it is no need to reactivate the materials by heating

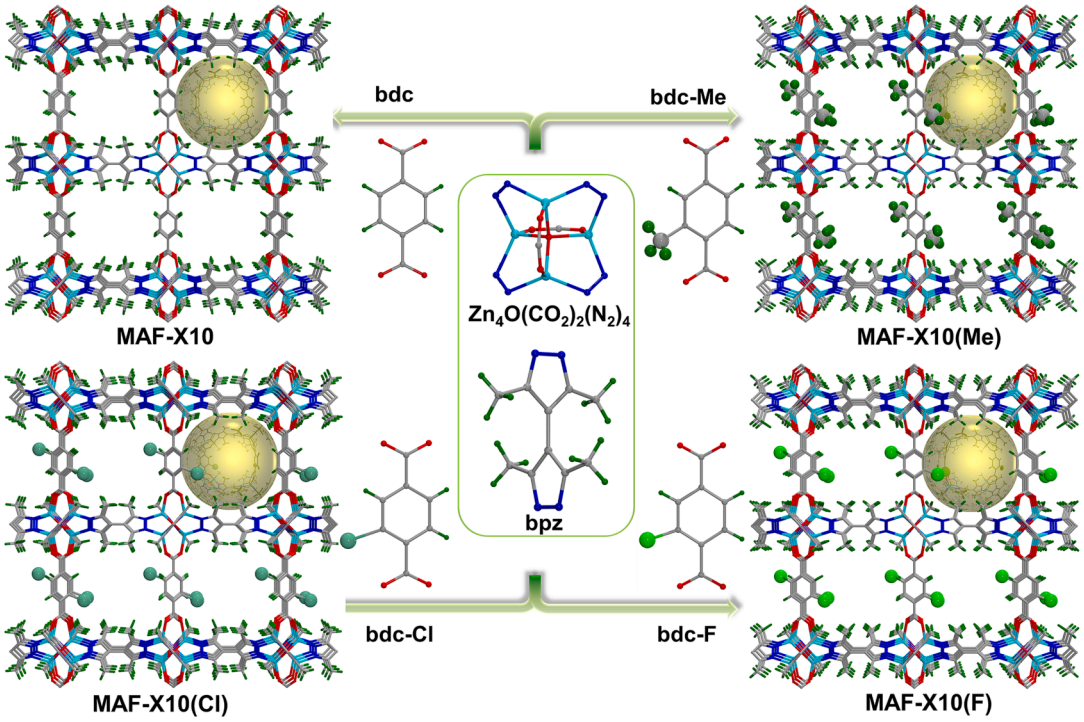

Fig. 1. Schematic representation of the constructions of MAF-X10, MAF-X10(Me), MAF-X10(Cl), and MAF-X10(F) from different substituent group-modified linkers.

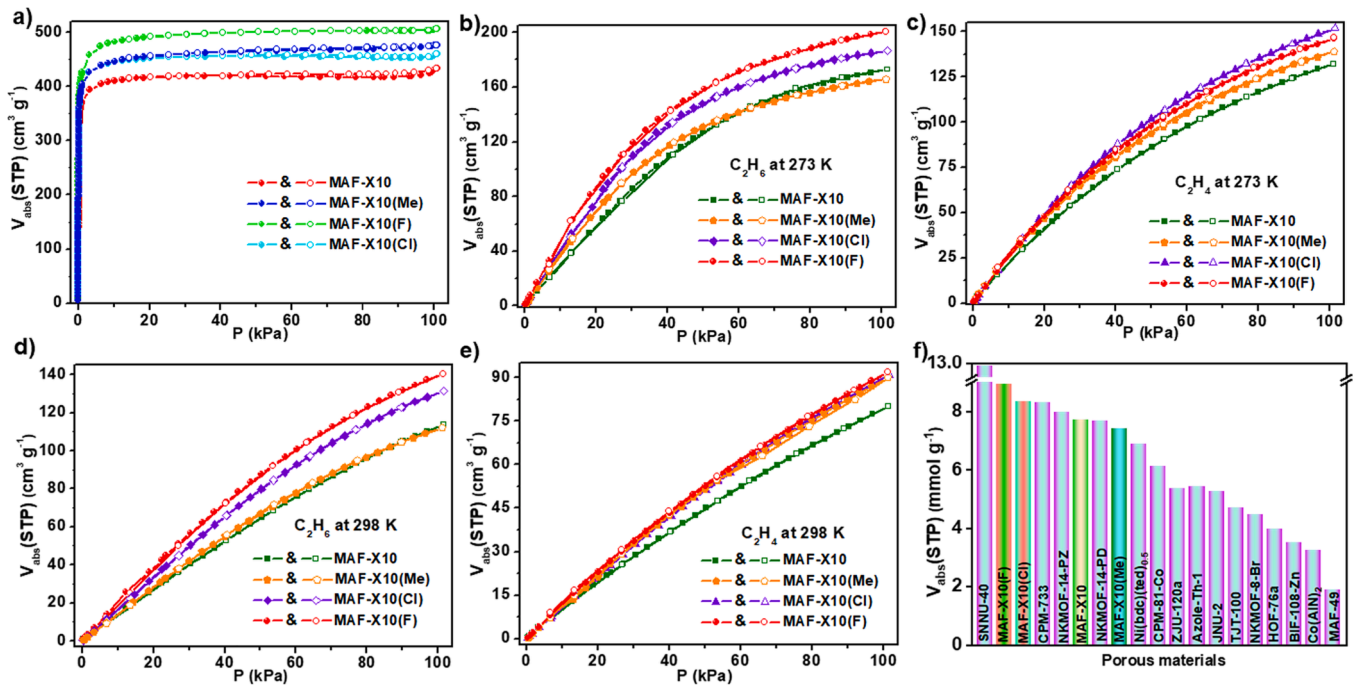

Fig. 2. A) N_2 sorption curves at 77 K; b) and d) C_2H_6 adsorption isotherms at 273 K and 298 K; c) and e) C_2H_4 adsorption isotherms at 273 K and 298 K; f) comparison of C_2H_6 uptakes at 273 K with reported C_2H_6-selective MOFs.

between each cycle, the fully reproducible C_2H_6 sorption curves can be obtained (Fig. S5). Moreover, the C_2H_6 adsorption isotherms of the MOFs treated by heating at 400 °C agreed well with the pristine material, illustrating good stability (Figs. S6 and S7).

3.4. Adsorption selectivity

To predict the separation feasibility of the MOFs for detaching trace C_2H_6 impurity from C_2H_6/C_2H_4 mixtures, ideal adsorbed solution theory (IAST) was applied to determine the selectivities for C_2H_6/C_2H_4 (1/1, 1/9, and 1/15, v/v) mixtures (Figs. S8–S11). As displayed in Fig. 3a and b, for the same MOF the IAST selectivities are almost similar for different C_2H_6/C_2H_4 compositions at 298/273 K, which were calculated to be about 1.5/1.6, 1.3/1.6, and 1.6/1.7 for MAF-X10, -X10(Me), and -X10 (Cl), respectively, while MAF-X10(F) displays higher selectivities of 1.8/2.1. Although these selectivities are not as good as some benchmark C_2H_6-selective MOFs, like $Fe_2(O_2)$(dobdc) (4.4) [29], Tb-MOF-76(NH_2) (2.1) [3], and $Cu(Qc)_2$ (3.4) [28], but are higher than or comparable to

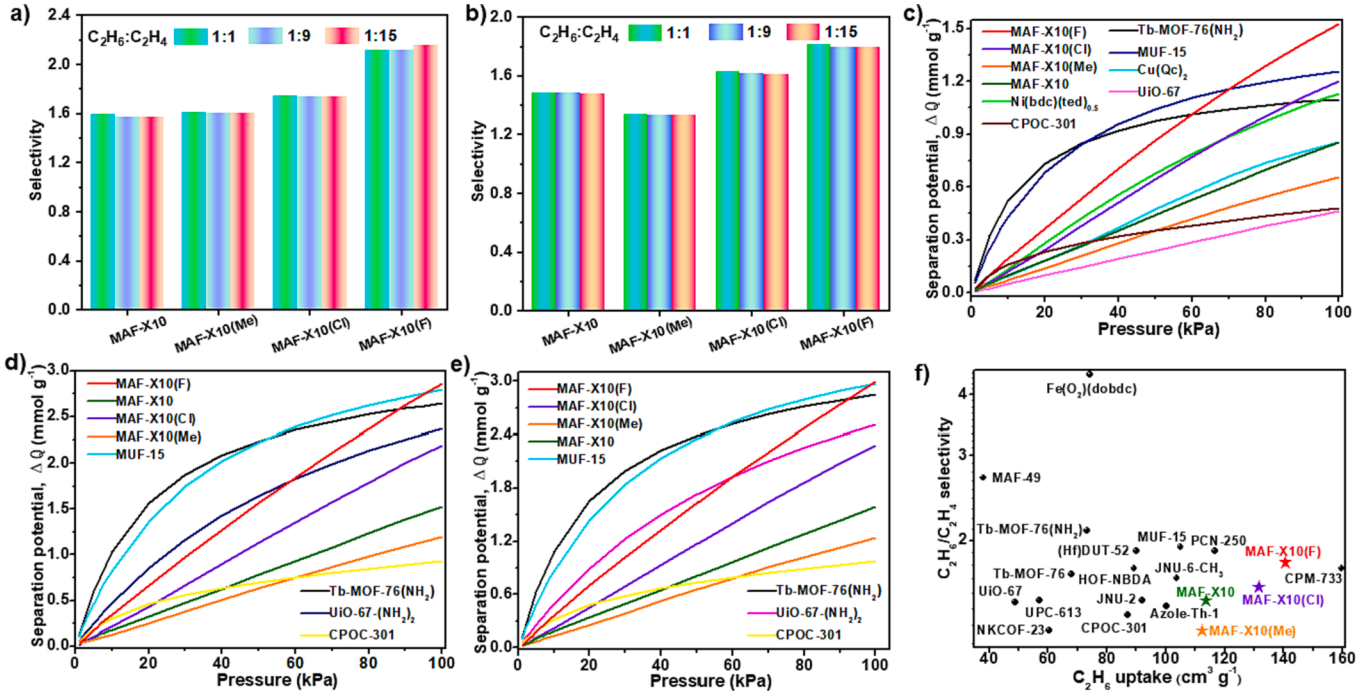

Fig. 3. A) and b) IAST selectivity of four mofs for c_2H_6-C_2H_4 mixtures at 273 K and 298 K under 100 kPa; separation potential of selected MOFs for C_2H_6/C_2H_4 mixtures: c) 1/1, d) 1/9, and e) 1/15; f) comparison of C_2H_6 adsorption uptake and C_2H_6/C_2H_4 selectivity in various MOFs at 298 K under 100 kPa.

some reported materials, such as HOF-NBDA (1.75) [31], JNU-6-CH_3 (1.67) [44], LIFM-63 (1.56) [45], TJT-100 (1.2) [46], [Zn_2(BDC)(H_2BPZ)$_{0.5}$(HBPZ)(BPZ)$_{0.5}$] (1.5) [35], and Zn-PNMI (1.42) [47]. At the same time, the separation potentials (ΔQ) represented by the maximum C_2H_4 amount that can be recovered from the C_2H_6/C_2H_4 mixtures were also calculated at 273 and 298 K, which is a combined selectivity-capacity metric [48–50]. As shown in Fig. 3c–e and S12a-c, for the different ratios (1/1, 1/9, and 1/15) of C_2H_6/C_2H_4 mixtures, MAF-X10 (F) showed more excellent ΔQ compared to MAF-X10, -X10(Me) and -X10(Cl). For example, for the 1/15 mixtures, the ΔQ of MAF-X10(F) is 2.99 mmol g^{-1}, which is significantly higher than MAF-X10 (1.59 mmol g^{-1}), -X10(Me) (1.24 mmol g^{-1}), and -X10(Cl) (2.28 mmol g^{-1}), and also greatly outperformed the advanced C_2H_6-selective materials Tb-MOF-76 (NH_2) (1.09 mmol g^{-1}) [3], CPOC-301 (0.48 mmol g^{-1}) [51], and MUF-15 (1.26 mmol g^{-1}) [25] under the same conditions. In addition, MAF-X10(F) also exhibited the largest C_2H_6/C_2H_4 uptake ratio (1.53) compared to other three MOFs (1.25–1.45). In general, in contrast with most MOFs, MAF-X10(F) exhibits very promising application for C_2H_6/C_2H_4 separation, in comprehensive consideration of C_2H_6 uptake, selectivity, and separation potential (Fig. 3f and Table S7).

3.5. Adsorption site

Grand Canonical Monte Carlo (GCMC) simulations were implemented to elucidate the origin of enhanced C_2H_6 uptake and C_2H_6/C_2H_4 selectivity in this MOF platform. It found that both C_2H_6 and C_2H_4 molecules were located in the nonpolar pockets surrounded by one tetranuclear SBU, two pyrazolates and one benzolate unit, as provided in Fig. 4. The C_2H_4 molecules in MAF-X10 and -X10(Me) interacted with two pyrazolates and one carboxylate group through C-H···π/N/O contacts, while C_2H_4 formed the C-H···π/N contacts in MAF-X10(Cl) and -X10(F). By contrast, the C_2H_6 molecule with more –CH units formed more contacts with the framework. In MAF-X10 and -X10(Me), the C_2H_6 molecule formed four C-H···N hydrogen bonds and two C-H···π interactions with two pyrazolate rings and three C-H···O hydrogen bonds with carboxylate groups and Zn_4O unit. Specially, for C_2H_6 molecule, MAF-X10(Cl) and -X10(F) not only formed C-H···π/N/O contacts, but also formed moderate C-H···Cl (H···Cl = 3.134 Å) or strong C-H···F (H···F = 2.767 Å) hydrogen bonds with accessible Cl and F sites in ligands. Thus, the binding strength of C_2H_6 with the framework follows the order: MAF-X10(F) > MAF-X10(Cl) > MAF-X10(Me) ≈ MAF-X10, coinciding with the single-component adsorption amounts and adsorption enthalpies. These results demonstrated the introduction of Cl and F sites in pore walls of MOFs was very effective to strengthen the interactions toward C_2H_6 as well as C_2H_6/C_2H_4 selectivity.

3.6. Breakthrough separation

To future assess the separation performance of MAF-X10 isomorphs in actual conditions, we carried out column breakthrough experiments, in which the simulated cracked gas feed of C_2H_6/C_2H_4 mixtures (5/5, 1/9, and 1/15, v/v) with Ar as the carrier gas (90 %, 90 %, and 84 %, vol %) were purged into the packed bed at 273 and 298 K under 1 atm (total flow rate = 5.0 mL min^{-1}). As depicted in Fig. 5a–c and S13a-c, these mixtures were efficiently separated by MAF-X10 isomorphs, wherein C_2H_4 gas was firstly eluted from the bed to directly gain a highly pure C_2H_4 (≥99.9 %), whereas C_2H_6 was completely adsorbed in the bed for a certain period of time. The breakthrough time difference (Δt) of two gases were 3.8, 5.1, 6.1 and 6.4 min g^{-1} for the 5/5 C_2H_6/C_2H_4 mixtures, 6.2, 7.0, 6.9, and 8.9 min g^{-1} for the 1/9 C_2H_6/C_2H_4 mixtures, as well as 5.4, 8.4, 9.1, and 9.9 min g^{-1} for the 1/15 C_2H_6/C_2H_4 mixtures, respectively, indicating a better separation performance for MAF-X10(F) than other isomorphs, matching well with the single-component adsorption uptakes. The dynamic selectivities on the basis of breakthrough curves for MAF-X10, -X10(Me), -X10(Cl), and -X10(F) were calculated to be 1.36, 1.32, 1.39, and 1.53 of 5/5 C_2H_6/C_2H_4 mixtures, 2.05, 1.97, 2.26, and 2.32 of 1/9 C_2H_6/C_2H_4 mixtures, as well as 1.67, 1.56, 1.97, and 2.28 of 1/15 C_2H_6/C_2H_4 mixtures at 298 K, respectively, which are consistent with the values predicted by IAST method.

Next, transient breakthrough simulations were performed for the exact same set of operating conditions as in the above mentioned experiments, using the methodology described in earlier publications by Krishna [48–50,52–54]. For MAF-X10(F), MAF-X10(Cl), and MAF-X10, there are good match between the experiments and simulations (Figs. S14–S16). For MAF-X10(Me), the experiments show better separation performance than anticipated by the breakthrough simulations (Fig. S17). Having established the accuracy of the transient breakthrough simulations, transient breakthrough simulations for the C_2H_6/C_2H_4 mixtures (50/50, 10/90, and 6.25/93.75, v/v) without inert gas were performed at 100 kPa and 298 K to further estimate the practical

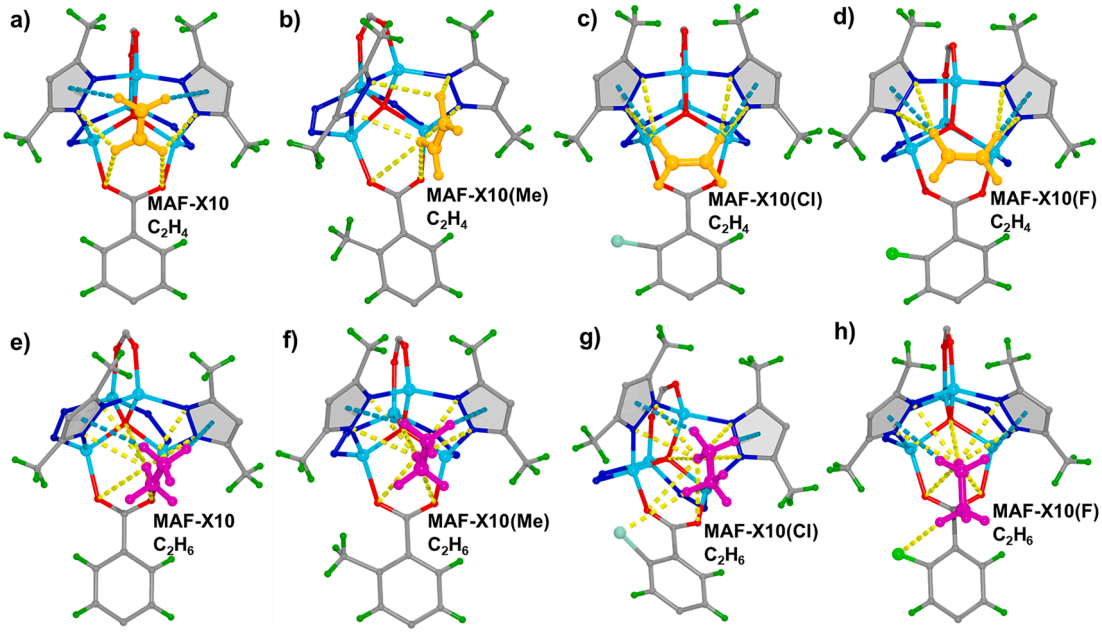

Fig. 4. a–d) C_2H_4 preferential adsorption sites in four isoreticular MOFs; e–h) C_2H_4 preferential adsorption sites in four isoreticular MOFs.

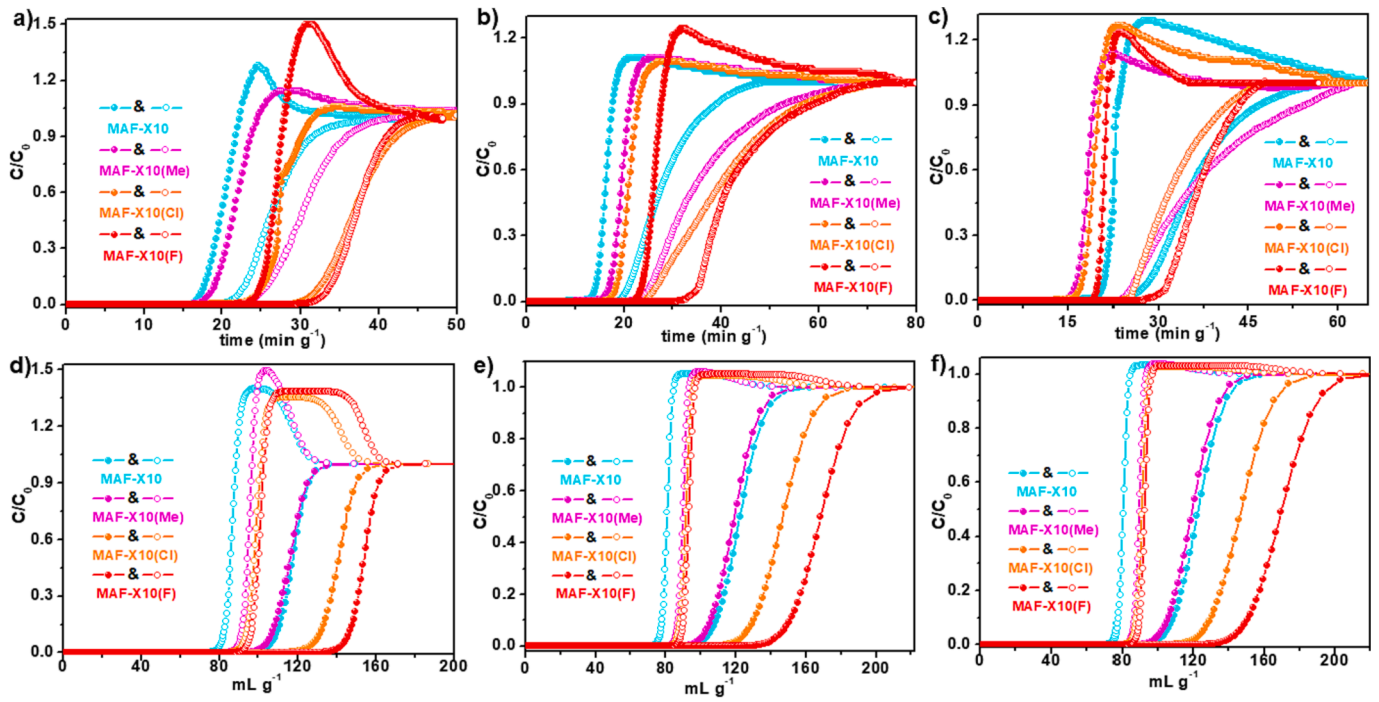

Fig. 5. Breakthrough curves for C_2H_6/C_2H_4 mixtures with Ar as carrier gas in four MOFs at 298 K and 100 kPa, a) (v/v, 5/5), b) (v/v, 1/9), c) (v/v, 1/15); transient breakthrough simulations without inert gas in four MOFs at 298 K and 100 kPa, d) (v/v, 50/50), e) (v/v, 10/90), f) (v/v, 6.25/93.75) (solid lines represent C_2H_4 and dashed lines represent C_2H_6).

separation performance and determine the C_2H_4 productivities of MAF-X10 isomorphs. The results in Fig. 5d–f indicate that four MOFs are capable of separating the three different concentrations of C_2H_6/C_2H_4 mixtures, in which MAF-X10(F) reveals an obviously better separation performance than MAF-X10 and MAF-X10(Me). Based on the simulated breakthrough curves, the productivities of ≥99.95 % pure C_2H_4 for 50/50, 10/90, and 6.25/93.75 C_2H_6/C_2H_4 mixtures are calculated to be 5.945, 17.685, and 19.628 L kg^{-1} of MAF-X10, respectively. The corresponding productivities for MAF-X10(Me) are 2.938, 4.278, and 6.663 L kg^{-1}, for MAF-X10(Cl) are 10.278, 25.641, and 29.602 L kg^{-1} and for MAF-X10(F) are 22.044, 43.965, and 47.874 L kg^{-1}, respectively (Table S8). It is worth noting that the C_2H_4 purity for 50/50 C_2H_6/C_2H_4 mixtures can only achieve 99.51 % purity. The value of 22.044 L kg^{-1} (≥99.95 %) for MAF-X10(F) is nearly 3.7 times for MAF-X10 with 5.945 L kg^{-1} (≥99.95 %), 5 times for $Cu(Qc)_2$ with 4.4 L kg^{-1} (>99.9 %) [28], 3.5 times for MAF-49 with 6.27 L kg^{-1} (>99.95 %) [27], 1.2 times for $Fe_2(O_2)$(dobdc) [29] with 18.59 L kg^{-1} (>99.95 %), and is comparable with the productivities of 22.06 L kg^{-1} (≥99.95 %) for JNU-6-CH_3 [41] and 21.1 L kg^{-1} (≥99.99 %) for JNU-2 [55].

Subsequently, the regeneration capability and reusability of MAF-X10 isomorphs were examined by multiple dynamic breakthrough tests for (5/5, v/v) C_2H_6/C_2H_4 mixtures under ambient conditions. The results in Fig. S18 indicated that the separation performance can be maintained for at least five continuous cycles. PXRD results proved that the stability of MAF-X10 isomorphs can be retained after multiple separation experiments. As shown in and Table 1, the polar sites-functionalized MAF-X10(Cl) and -X10(F) significantly improved C_2H_6/C_2H_4 separation performance including IAST selectivity, separation potential, C_2H_4 productivity as well as adsorption amount, adsorption enthalpy and breakthrough time of C_2H_6. This significantly improved separation performance confirms that installing polar sites in nonpolar pore is an effective approach for MOF designs addressing the challenging separation.

Overall, the excellent adsorption properties and efficient C_2H_6/C_2H_4 separation performance make MAF-X10 materials be the outstanding adsorbents for C_2H_4 purification. Notably, the separation of C_2H_6/C_2H_4 in real application would be very complex due to the existence of other gas byproducts, which could influence the separation effect of C_2H_6/C_2H_4 in a degree. Before any porous adsorbents can be realized for the challenging real cracking gas separation, step-by-step separations by different adsorbents will be necessary to obtain high purity C_2H_4 products.

Table 1
Comparison of adsorption for C_2H_6 and C_2H_4 gases and separation performance for C_2H_6/C_2H_4 mixtures (v/v, 5/5) in four MOFs at 298 K under 100 kPa.

MOFs	Uptake, C_2H_6 *vs* C_2H_4 ($cm^3\ g^{-1}$)	Selectivity	ΔQ (mmol/g)	Q_{st}, C_2H_6 *vs* C_2H_4 (kJ/mol)	C_2H_4 productivity (L kg^{-1})
MAF-X10	113.6 *vs* 80.0	1.5	0.86	23.4 *vs* 22.4	5.945
MAF-X10 (Me)	112.2 *vs* 89.9	1.3	0.66	26.7 *vs* 21.2	2.938
MAF-X10 (Cl)	131.5 *vs* 90.7	1.6	1.20	25.0 *vs* 23.5	10.278
MAF-X10 (F)	140.5 *vs* 91.7	1.8	1.53	24.9 *vs* 21.7	22.044

4. Conclusions

In summary, a series of isoreticular MOF material platforms with finely-tuned pore environments were judiciously constructed based on the reticular chemistry principle to systematically evaluate the effect of installing polar adsorption sites in nonpolar pore environment for C_2H_6/C_2H_4 separation. Owing to the methyl group-modified nonpolar pore environment, four MOFs displayed impressive C_2H_6-selective behavior with high ad-sorption uptakes (>110 $cm^3\ g^{-1}$). Specially, MAF-X10(F) with polar F adsorption sites exhibited the highest C_2H_6 uptake (140.5 $cm^3\ g^{-1}$) among the four MOFs, which ranked the top among the

reported C_2H_6-selective MOFs. In contrast, MAF-X10(Me) modified by methyl groups showed the similar C_2H_6 uptake with parent MAF-X10, which further confirmed the fact that polar sites were highly favoured in C_2H_6 adsorption. The four MOFs can efficiently achieve one-step C_2H_4 purification from various ratios of C_2H_6/C_2H_4 mixtures with great recyclability. The polar sites-functionalized MAF-X10(Cl) and MAF-X10 (F) significantly improved C_2H_6/C_2H_4 separation in comprehensive of IAST selectivity, separation potential, C_2H_4 productivity, gas uptake, adsorption enthalpies. Molecular simulations indicated that the formation of strong C-H···Cl/F interactions between the polar adsorption sites (Cl or F) of MAF-X10(Cl), (F) and C_2H_6 mainly contributed to increased C_2H_6/C_2H_4 separation. The design principle of installing polar adsorption sites in the nonpolar pore environment is general, and will provide an important strategy to facilitate the rational design and implementation of MOF materials for C_2H_6/C_2H_4 separation challenges.

CRediT authorship contribution statement

Gang-Ding Wang: Writing – original draft, Funding acquisition. **Yong-Zhi Li:** Writing – review & editing, Formal analysis. **Rajamani Krishna:** Methodology. **Zhi-Zhu Yan:** Formal analysis. **Lei Hou:** Writing – review & editing, Supervision, Funding acquisition, Formal analysis. **Yao-Yu Wang:** Resources. **Zhonghua Zhu:** Software.

Declaration of competing interest

The authors declare that they have no known competing financial interests or personal relationships that could have appeared to influence the work reported in this paper.

Data availability

The data will be made available in Supporting Information

Acknowledgements

This work is supported by National Nature Science Foundation of China (22371226 and 22371225), Natural Science Basic Research Program of Shaanxi (2024JC-JCQN-18), and Cultivation Program for the Excellent Doctoral Dissertation of Northwest University (YB2023005).

Appendix A. Supplementary data

Supplementary data to this article can be found online at https://doi.org/10.1016/j.cej.2024.149587.

References

[1] H. Zimmermann, R. Walzl, Ullmann's Encyclopedia of Industrial Chemistry, Wiley, 2009.
[2] Q. Hong, W. Wang, S. Chen, K. Chen, M. Liu, H.-X. Zhang, J. Zhang, Host-guest pore space partition in a boron imidazolate framework for ethylene separation, Chem. Mater. 34 (2022) 307–313.
[3] G.-D. Wang, R. Krishna, Y.-Z. Li, W.-J. Shi, L. Hou, Y.-Y. Wang, Z. Zhu, Boosting ethane/ethylene separation by MOFs through the amino-functionalization of pores, Angew. Chem. Int. Ed. 61 (2022) e202213015.
[4] R.-B. Lin, L. Li, H.-L. Zhou, H. Wu, C. He, S. Li, R. Krishna, J. Li, W. Zhou, B. Chen, Molecular sieving of ethylene from ethane using a rigid metal-organic framework, Nat. Mater. 17 (2018) 1128–1133.
[5] P. Zhang, Y. Zhong, Y. Zhang, Z. Zhu, Y. Liu, Y. Su, J. Chen, S. Chen, Z. Zeng, H. Xing, S. Deng, J. Wang, Synergistic binding sites in a hybrid ultramicroporous material for one-step ethylene purification from ternary C_2 hydrocarbon mixture, Sci. Adv. 8 (2022) eabn9231.
[6] S. Geng, E. Lin, X. Li, W. Liu, T. Wang, Z. Wang, D. Sensharma, S. Darwish, Y. H. Andaloussi, T. Pham, P. Cheng, M.J. Zaworotko, Y. Chen, Z. Zhang, Scalable room-temperature synthesis of highly robust ethane-selective metal-organic frameworks for efficient ethylene purification, J. Am. Chem. Soc. 143 (2021) 8654–8660.
[7] S. Jiang, J. Li, M. Feng, R. Chen, L. Guo, Q. Xu, L. Chen, F. Shen, Z. Zhang, Y. Yang, Q. Ren, Q. Yang, Z. Bao, Hydrophobic paraffin-selective pillared-layer MOFs for olefin purification, J. Mater. Chem. A 10 (2022) 24127–24136.
[8] Z. Xu, X. Xiong, J. Xiong, R. Krishna, L. Li, Y. Fan, F. Luo, B. Chen, A robust Th-azole framework for highly efficient purification of C_2H_4 from a $C_2H_4/C_2H_2/C_2H_6$ mixture, Nat. Commun. 11 (2020) 3163.
[9] Y. Yang, L. Li, R.-B. Lin, Y. Ye, Z. Yao, L. Yang, F. Xiang, S. Chen, Z. Zhang, S. Xiang, B. Chen, Ethylene/ethane separation in a stable hydrogen-bonded organic framework through a gating mechanism, Nat. Chem. 13 (2021) 933–939.
[10] Y. Jiang, Y. Hu, B. Luan, L. Wang, R. Krishna, H. Ni, X. Hu, Y. Zhang, Benchmark single-step ethylene purification from ternary mixtures by a customized fluorinated anion-embedded MOF, Nat. Commun. 14 (2023) 401.
[11] Y. Xie, Y. Shi, E.M. Cedeño Morales, A.E. Karch, B. Wang, H. Arman, K. Tan, B. Chen, Optimal binding affinity for sieving separation of propylene from propane in an oxyfluoride anion-based metal-organic framework, J. Am. Chem. Soc. 145 (2023) 2386–2394.
[12] Y. Wang, M. Fu, S. Zhou, H. Li, X. Wang, W. Fan, Z. Liu, Z. Wang, D. Li, H. Hao, X. Lu, S. Hu, D. Sun, Guest-molecule-induced self-adaptive pore engineering facilitates purification of ethylene from ternary mixture, Chem 8 (2022) 3263–3274.
[13] H. Zeng, M. Xie, T. Wang, R.-J. Wei, X.-J. Xie, Y. Zhao, W. Lu, D. Li, Orthogonal-array dynamic molecular sieving of propylene/propane mixtures, Nature 595 (2021) 542–548.
[14] X.-J. Xie, H. Zeng, W. Lu, D. Li, Meta-organic frameworks for hydrocarbon separation: design, progress, and challenges, J. Mater. Chem. A 11 (2023) 20459–20469.
[15] M. Shivanna, K.-I. Otake, B.-Q. Song, L.M. van Wyk, Q.-Y. Yang, N. Kumar, W. K. Feldmann, T. Pham, S. Suepaul, B. Space, L.J. Barbour, S. Kitagawa, M. J. Zaworotko, Benchmark acetylene binding affinity and separation through induced fit in a flexible hybrid ultramicroporous material, Angew. Chem. Int. Ed. 60 (2021) 20383–20390.
[16] W. Gong, Y. Xie, X. Wang, K.O. Kirlikovali, K.B. Idrees, F. Sha, H. Xie, Y. Liu, B. Chen, Y. Cui, O.K. Farha, Programmed polarizability engineering in a cyclen-based cubic Zr(IV) metal-organic framework to boost Xe/Kr separation, J. Am. Chem. Soc. 145 (2023) 2679–2689.
[17] F. Zheng, R. Chen, Y. Liu, Q. Yang, Z. Zhang, Y. Yang, Q. Ren, Z. Bao, Strengthening Intraframework Interaction within Flexible MOFs demonstrates simultaneous sieving acetylene from ethylene and carbon dioxide, Adv. Sci. 10 (2023) 2207127.
[18] H. Zeng, X.-J. Xie, Y. Wang, D. Luo, R.-J. Wei, W. Lu, D. Li, Spatial disposition of square-planar mononuclear nodes in metal–organic frameworks for C_2H_2/CO_2 separation, Chem. Sci. 13 (2022) 12876–12882.
[19] Y. Wang, T. Li, L. Li, R.-B. Lin, X. Jia, Z. Chang, H.-M. Wen, X.-M. Chen, J. Li, Construction of fluorinated propane-trap in metal-organic frameworks for record polymer-grade propylene production under high humidity conditions, Adv. Mater. 35 (2023) 220795.
[20] C. Jiang, C. Hao, X. Wang, H. Liu, X. Wei, H. Xu, Z. Wang, Y. Ouyang, W. Guo, F. Dai, D. Sun, Constructing C_2H_2 anchoring traps within MOF interpenetration nets as C_2H_2/CO_2 and C_2H_2/C_2H_4 bifunctional separator, Chem. Eng. J. 453 (2023) 139713.
[21] W. Fan, S. Yuan, W. Wang, L. Feng, X. Liu, X. Zhang, X. Wang, Z. Kang, F. Dai, D. Yuan, D. Sun, H.-C. Zhou, Optimizing multivariate metal-organic frameworks for efficient C_2H_2/CO_2 separation, J. Am. Chem. Soc. 142 (2020) 8728–8737.
[22] K.-J. Chen, D. G. Madden, S. Mukherjee, T. Pham, K. A. Forrest, A. Kumar, B. Space, J. Kong, Q.-Y. Zhang, M, J. Zaworotko, Synergistic sorbent separation for one-step ethylene purification from a four-component mixture, Science 366 (2019) 241-246.
[23] T. Lan, L. Li, Y. Chen, X. Wang, J. Yang, J. Li, Opportunities and critical factors of porous metal-organic frameworks for industrial light olefins separation, Mater. Chem. Front. 4 (2020) 1954–1984.
[24] H. Wang, D. Luo, E. Velasco, L. Yu, J. Li, Separation of alkane and alkene mixtures by metal-organic frameworks, J. Mater. Chem. A 9 (2021) 20874–20896.
[25] O.T. Qazvini, R. Babarao, Z.-L. Shi, Y.-B. Zhang, S.G. Telfer, A robust ethane-trapping metal-organic framework with a high capacity for ethylene purification, J. Am. Chem. Soc. 141 (2019) 5014–5020.
[26] C. Gücüyener, J. Bergh, J. Gascon, F. Kapteijn, Ethane/ethene separation turned on its head: selective ethane adsorption on the metal-organic framework ZIF-7 through a gate-opening mechanism, J. Am. Chem. Soc. 132 (2010) 17704–17706.
[27] P.-Q. Liao, W.-X. Zhang, J.-P. Zhang, X.-M. Chen, Efficient purification of ethene by an ethane-trapping metal-organic framework, Nat. Commun. 6 (2015) 8697.
[28] R.-B. Lin, H. Wu, L. Li, X.-L. Tang, Z. Li, J. Gao, H. Cui, W. Zhou, B. Chen, Boosting ethane/ethylene separation within isoreticular ultramicroporous metal-organic frameworks, J. Am. Chem. Soc. 140 (2018) 12940–12946.
[29] L. Li, R.-B. Lin, R. Krishna, H. Li, S. Xiang, H. Wu, J. Li, W. Zhou, B. Chen, Ethane/ethylene separation in a metal-organic framework with iron-peroxo sites, Science 362 (2018) 443–446.
[30] O.M. Yaghi, Reticular chemistry-construction, properties, and precision reactions of frameworks, J. Am. Chem. Soc. 138 (2016) 15507–15509.
[31] Y. Zhou, C. Chen, R. Krishna, Z. Ji, D. Yuan, M. Wu, Tuning pore polarization to boost ethane/ethylene separation performance in hydrogen-bonded organic frameworks, Angew. Chem. Int. Ed. 62 (2023) e202305041.
[32] M.-H. Yu, H. Fang, H.-L. Huang, M. Zhao, Z.-Y. Su, H.-X. Nie, Z. Chang, T.-L. Hu, Tuning the trade-off between ethane/ethylene selectivity and adsorption capacity within isoreticular microporous metal-organic frameworks by linker fine-fluorination, Small 19 (2023) 2300821.
[33] G.-D. Wang, J. Chen, Y.-Z. Li, L. Hou, Y.-Y. Wang, Z. Zhu, A robust ethane-selective metal-organic framework with nonpolar pore surface for efficient C_2H_6/C_2H_4 separation, Chem. Eng. J. 433 (2022) 133786.
[34] Z. Di, C. Liu, J. Pang, S. Zou, Z. Ji, F. Hu, C. Chen, D. Yuan, M. Hong, M. Wu, A metal-organic framework with nonpolar pore surfaces for the one-step

acquisition of C_2H_4 from a C_2H_4 and C_2H_6 mixture, Angew. Chem. Int. Ed. 61 (2022) e202210343.
[35] A.E. Amooghin, H. Sanaeepur, R. Luque, H. Garcia, B. Chen, Fluorinated metal-organic frameworks for gas separation, Chem. Soc. Rev. 51 (2022) 7427–7508.
[36] X.-Q. Wu, J.-H. Liu, T. He, P.-D. Zhang, J. Yu, J.-R. Li, Understanding how pore surface fluorination influences light hydrocarbon separation in metal-organic frameworks, Chem. Eng. J. 407 (2021) 127183.
[37] L. Hou, Y.-Y. Lin, X.-M. Chen, Porous metal-organic framework based on μ_4-oxo tetrazinc clusters: sorption and guest-dependent luminescent properties, Inorg. Chem. 47 (2008) 1346–1351.
[38] C. Serre, Superhydrophobicity in highly fluorinated porous metal-organic frameworks, Angew. Chem. Int. Ed. 51 (2012) 6048–6050.
[39] P. Küsgens, M. Rose, I. Senkovska, H. Fröde, A. Henschel, S. Siegle, S. Kaskel, Characterization of metal-organic frameworks by water adsorption, Micropor. Mesopor. Mater. 120 (2009) 325–330.
[40] G.-D. Wang, R. Krishna, Y.-Z. Li, Y.-Y. Ma, L. Hou, Y.-Y. Wang, Z. Zhu, Rational construction of ultrahigh thermal stable MOF for efficient separation of MTO products and natural gas, ACS Materials Lett. 5 (2023) 1091–1099.
[41] Y.-P. Li, Y.-N. Zhao, S.-N. Li, D.-Q. Yuan, Y.-C. Jiang, X. Bu, M.-C. Hu, Q.-G. Zhai, Ultrahigh-uptake capacity-enabled gas separation and fruit preservation by a new single-walled nickel-organic framework, Adv. Sci. 8 (2021) 2003141.
[42] H. Yang, Y. Wang, R. Krishna, X. Jia, Y. Wang, A.N. Hong, C. Dang, H.E. Castillo, X. Bu, P. Feng, Pore-space-partition-enabled exceptional ethane uptake and ethane-selective ethane-ethylene separation, J. Am. Chem. Soc. 142 (2020) 2222–2227.
[43] H. Xiang, Y. Shao, A. Ameena, H. Chen, W. Yang, P. Gorgojo, F.R. Siperstein, X. Fan, Q. Pan, Adsorptive separation of C2H6/C2H4 on metal-organic frameworks (MOFs) with pillared-layer structures, Sep. Purif. Technol. 242 (2020) 11681.
[44] X.-J. Xie, Y. Wang, Q.-Y. Cao, R. Krishna, H. Zeng, W. Lu, D. Li, Surface engineering on a microporous metal-organic framework to boost ethane/ethylene separation under humid conditions, Chem. Sci. 14 (2023) 11890–11895.
[45] C.-X. Chen, Z.-W. Wei, T. Pham, P.C. Lan, L. Zhang, K.A. Forrest, S. Chen, A.M. Al-Enizi, A. Nafady, C.-Y. Su, S. Ma, Nanospace engineering of metal-organic frameworks through dynamic spacer installation of multi-functionalities for efficient separation of ethane from ethane/ethylene mixture, Angew. Chem. Int. Ed. 60 (2021) 9680–9685.
[46] H.-G. Hao, Y.-F. Zhao, D.-M. Chen, J.-M. Yu, K. Tan, S. Ma, Y. Chabal, Z.-M. Zhang, J.-M. Dou, Z.-H. Xiao, G. Day, H.-C. Zhou, T.-B. Lu, Simultaneous trapping of C_2H_2 and C_2H_6 from a ternary mixture of $C_2H_2/C_2H_4/C_2H_6$ in a robust metal-organic framework for the purification of C_2H_4, Angew. Chem. Int. Ed. 57 (2018) 16067–16071.
[47] L. Yang, Y. Wang, Y. Chen, J. Yang, X. Wang, L. Li, J. Li, Microporous metal-organic framework with specific functional sites for efficient removal of ethane from ethane/ethylene mixtures, Chem. Eng. J. 387 (2020) 124137.
[48] R. Krishna, Screening metal-organic frameworks for mixture separations in fixed-bed adsorbers using a combined selectivity/capacity metric, RSC Adv. 7 (2017) 35724–35737.
[49] R. Krishna, Methodologies for screening and selection of crystalline microporous materials in mixture separations, Sep. Purif. Technol. 194 (2018) 281–300.
[50] R. Krishna, Metrics for evaluation and screening of metal-organic frameworks for applications in mixture separations, ACS Omega 5 (2020) 16987–17004.
[51] K. Su, W. Wang, S. Du, C. Ji, D. Yuan, Efficient ethylene purification by a robust ethane-trapping porous organic cage, Nat. Commun. 13 (2021) 370.
[52] R. Krishna, The Maxwell-Stefan description of mixture diffusion in nanoporous crystalline materials, Microporous Mesoporous Mater. 185 (2014) 30–50.
[53] R. Krishna, Methodologies for evaluation of metal-organic frameworks in separation applications, RSC Adv. 5 (2019) 52269–52295.
[54] R. Krishna, Synergistic and antisynergistic intracrystalline diffusional influences on mixture separations in fixed bed adsorbers, Precision Chemistry 1 (2023) 83–93.
[55] H. Zeng, X.-J. Xie, M. Xie, Y.-L. Huang, D. Luo, T. Wang, Y. Zhao, W. Lu, D. Li, Cage-interconnected metal-organic framework with tailored apertures for efficient C_2H_6/C_2H_4 separation under humid conditions, J. Am. Chem. Soc. 141 (2019) 20390–20396.

Supporting Information

Fine-tuning the Pore Environment of Isoreticular Metal-Organic Frameworks through Installing Functional Sites for Boosting C_2H_6/C_2H_4 Separation

Gang-Ding Wang[a], Yong-Zhi Li[c],* Rajamani Krishna,[b] Zhi-Zhu Yan [a], Lei Hou[a],* Yao-Yu Wang[a], and Zhonghua Zhu[c]

[a]Key Laboratory of Synthetic and Natural Functional Molecule of the Ministry of Education, Shaanxi Key Laboratory of Physico-Inorganic Chemistry, College of Chemistry & Materials Science, Northwest University, Xi'an 710069, P. R. China.

[b]Van 't Hoff Institute for Molecular Sciences University of Amsterdam Science Park 904, 1098 XH Amsterdam, The Netherlands.

[c]School of Materials and Physics, China University of Mining and Technology Xuzhou 221116, P. R. China.

[d]School of Chemical Engineering, The University of Queensland, Brisbane 4072, Australia.

*To whom correspondence should be addressed. E-mail: Lyz2021@cumt.edu.cn (Yong-Zhi Li); lhou2009@nwu.edu.cn (Lei Hou).

Materials and general methods

All solvents and organic ligand for synthesis were purchased commercially. Elemental analyses of C, H, and N were determined with a Perkin-Elmer 2400C elemental analyzer. Thermalgravimetric analyses (TGA) were carried out in a nitrogen stream using a Netzsch TG209F3 equipment at a heating rate of 10 °C min^{-1}. Single crystal diffraction data were collected on a Bruker SMART APEX II CCD single crystal diffractometer. Gas adsorption measurements were performed with an automatic volumetric sorption apparatus (Micrometrics ASAP 2020M), in which the sample was activated by immersing in CH_2Cl_2 for 72 hours and then heating at 393 K under vacuum for 4 hours. Water sorption was collected by Quantachrome Vstar vapor adsorption equipment. Breakthrough experiments were performed on a Quantachrome dynaSorb BT equipments.

X-ray crystallography

A Bruker Smart Apex II CCD detector was used to collect the single crystal data at 180(2) or 174(2) K using Mo Kα radiation (λ = 0.71073 Å). The structure was solved by direct methods and refined by full-matrix least-squares refinement based on F2 with the SHELXTL program. The non-hydrogen atoms were refined anisotropically with the hydrogen atoms added at their geometrically ideal positions and refined isotropically. As the disordered solvent molecules in the structure cannot be located, the SQUEEZE routine of Platon program was applied in refining. The formula of complex was got by the single crystal analysis together with elemental microanalyses and TGA data. Relevant crystallographic results were listed in Table S5. Selected bond lengths and angles were provided in Table S6.

Fitting of unary isotherm data

The unary isotherms for C_2H_6, and C_2H_4, measured at two different temperatures 273 K, and 298 K in MAF-X10(F), MAF-X10(Cl), MAF-X10(Me), and MAF-X10 were fitted with excellent accuracy using the 1-site Langmuir-Freundlich model:

$$q = \frac{q_{sat} b p^{v}}{1 + b p^{v}} \qquad \text{(S1)}$$

In eq (S1), the Langmuir-Freundlich parameter b is temperature dependent

$$b = b_0 \exp\left(\frac{E}{RT}\right) \quad \text{(S2)}$$

In eq (S2), E is the energy parameter. The unary isotherm fit parameters are provided in Table S1, Table S2, Table S3, and Table S4,

Isosteric heat of adsorption

The isosteric heat of adsorption, Q_{st}, is defined as

$$Q_{st} = -RT^2\left(\frac{\partial \ln p}{\partial T}\right)_q \quad \text{(S3)}$$

where, the derivative in the right member of eq (S3) is determined at constant adsorbate loading, q. the derivative was determined by analytic differentiation of the combination of eq (S1), eq (S2), and eq (S3).

Table S1. 1-site Langmuir-Freundlich fits for C_2H_6 and C_2H_4 in MAF-X10(F).

	$\frac{q_{sat}}{\text{mol/kg}}$	$\frac{b_0}{\text{Pa}^{-1}}$	$\frac{E}{\text{kJ mol}^{-1}}$	ν
C_2H_6	14	3.322E-10	24.9	1
C_2H_4	13.5	6.665E-10	21.7	1

Table S2. 1-site Langmuir-Freundlich fits for C_2H_6 and C_2H_4 in MAF-X10(Cl).

	$\frac{q_{sat}}{\text{mol/kg}}$	$\frac{b_0}{\text{Pa}^{-1}}$	$\frac{E}{\text{kJ mol}^{-1}}$	ν
C_2H_6	11.5	3.081E-11	28	1.12
C_2H_4	14.5	2.847E-10	23.5	1

Table S3. 1-site Langmuir-Freundlich fits for C_2H_6 and C_2H_4 in MAF-X10(Me).

	$\frac{q_{sat}}{\text{mol/kg}}$	$\frac{b_0}{\text{Pa}^{-1}}$	$\frac{E}{\text{kJ mol}^{-1}}$	ν
C_2H_6	10.7	2.589E-11	29	1.085
C_2H_4	13	8.232E-10	21.2	1

Table S4. 1-site Langmuir-Freundlich fits for C_2H_6 and C_2H_4 in MAF-X10.

	$\frac{q_{sat}}{\text{mol/kg}}$	$\frac{b_0}{\text{Pa}^{-1}}$	$\frac{E}{\text{kJ mol}^{-1}}$	v
C_2H_6	14.7	3.950E-10	23.4	1
C_2H_4	12.8	4.449E-10	22.4	1

Gas selectivity prediction via IAST

The experimental isotherm data for pure C_2H_4 and C_2H_6 were fitted using a dual Langmuir-Freundlich (L-F) model:

$$q = \frac{a_1 * b_1 * P^{c_1}}{1 + b_1 * P^{c_1}} + \frac{a_2 * b_2 * P^{c_2}}{1 + b_2 * P^{c_2}}$$

Where q and p are adsorbed amounts and the pressure of component i, respectively.

The adsorption selectivities for binary mixtures defined by

$$S_{i/j} = \frac{x_i * y_j}{x_j * y_i}$$

were respectively calculated using the Ideal Adsorption Solution Theory (IAST). Where *xi* is the mole fraction of component *i* in the adsorbed phase and *yi* is the mole fraction of component *i* in the bulk.

Breakthrough experiments

The breakthrough experiment was performed on the Quantachrome dynaSorb BT equipments at 298 K and 1 bar with an equal volume of mixed gas (gas A: gas B: Ar = 5% : 5% : 90%, Ar as the carrier gas, flow rate = 5 mL min^{-1}). The activated MOFs (about 0.65 g) were filled into a packed column of ϕ 4.2×80 mm, and then the packed column was washed with Ar at a rate of 7 mL min^{-1} at 333 K for 35 minutes to further activate the samples. Between two breakthrough experiments, the adsorbent was regenerated by Ar flow of 7 mL min^{-1} for 35 min at 333 K to guarantee a complete removal of the adsorbed gases.

Molecular simulations

Grand canonical Monte Carlo (GCMC) simulations were performed for the gas adsorption in the framework by the Sorption module of Material Studio (Accelrys. Materials Studio Getting Started). The framework was considered to be rigid, and the optimized gas molecules were used. The partial charges for atoms of the framework were derived from QEq method

and QEq neutral 1.0 parameter. One unit cell was used during the simulations. The interaction energies between the gas molecules and framework were computed through the Coulomb and Lennard-Jones 6-12 (LJ) potentials. All parameters for the atoms were modeled with the universal force field (UFF) embedded in the MS modeling package. A cutoff distance of 12.5 Å was used for LJ interactions, and the Coulombic interactions were calculated by using Ewald summation. For each run, the 5×10^6 maximum loading steps, 5×10^6 production steps were employed.

Transient breakthrough simulations *vs* experiments with inert gas

The transient breakthrough experiments were conducted with mass of MAF-X10(F), MAF-X10(Cl), MAF-X10(Me), and MAF-X10 m_{ads}= 0.65 g; length of packed bed, L = 80 mm; inner diameter of packed bed= 4.2 mm. The mixtures examined were: C_2H_6/C_2H_4/Ar mixtures (5/5/90, 1/9/90, and 1/15/84, v/v/v) with Ar as the carrier gas, and a total flow rate of 5 mL min^{-1} (298 K, 100 kPa).

Transient breakthrough simulations were carried out for the exact same set of operating conditions as in the above mentioned experiments, using the methodology described in earlier publications.[1-6] In these simulations, intra-crystalline diffusion influences are ignored. For MAF-X10(F), MAF-X10(Cl), and MAF-X10, there is good match between the experiments and simulations. For MAF-X10(Me), the experiments show better separation performance than anticipated by the breakthrough simulations.

Transient breakthrough simulations without inert gas

Having established the accuracy of the transient breakthrough simulations, a set of simulations were carried out without inert gas in a fixed bed packed with MAF-X10(F), MAF-X10(Cl), MAF-X10(Me), and MAF-X10 m_{ads} = 0.65 g; length of packed bed, L = 80 mm; inner diameter of packed bed= 4.2 mm. The total pressure is 100 kPa, and two different temperatures were used: 298 K. The following mixtures were simulated.

50/50 C_2H_6(1)/C_2H_4(2) mixtures

10/90 C_2H_6(1)/C_2H_4(2) mixtures

6.25/97.5 C_2H_6(1)/C_2H_4(2) mixtures

The breakthrough data are presented in terms of the dimensionless concentrations at the exit

of the fixed bed, $\frac{c_A}{c_{A0}}$, as function of the modified time parameter $\frac{(Q_0 = flow\ rate\ mL\ min^{-1}) \times (time\ in\ min)}{(g\ MOF\ packed\ in\ tube)} = \frac{Q_0 t}{m_{ads}} = mL\ g^{-1}$.

Notation

b	Langmuir-Freundlich constant, Pa^{-v}
E	energy parameter, J mol^{-1}
L	length of packed bed adsorber, m
m_{ads}	mass of adsorbent packed in fixed bed, kg
p_i	partial pressure of species i, Pa
q_i	component molar loading of species i, mol kg^{-1}
q_{sat}	saturation loading, mol kg^{-1}
Q_0	volumetric flow rate of gas mixture entering fixed bed, $m^3\ s^{-1}$
Q_{st}	isosteric heat of adsorption, J mol^{-1}
T	absolute temperature, K

Greek letters

ν	Freundlich exponent, dimensionless
ρ	framework density, kg m^{-3}

Molecular structure					
Molecular formula	**Molecular Dimension (Å)** *X*	*Y*	*Z*	**Kinetic diameter (Å)**	**Polari × 10^{-25} (cm^{-3})**	**Boiling point(K)**
C_2H_4	3.28	4.18	4.84	4.16	42.5	169.4
C_2H_6	3.81	4.08	4.82	4.44	44.3-44.7	184.6

Scheme S1. Structures and physical properties of C_2H_4 and C_2H_6.

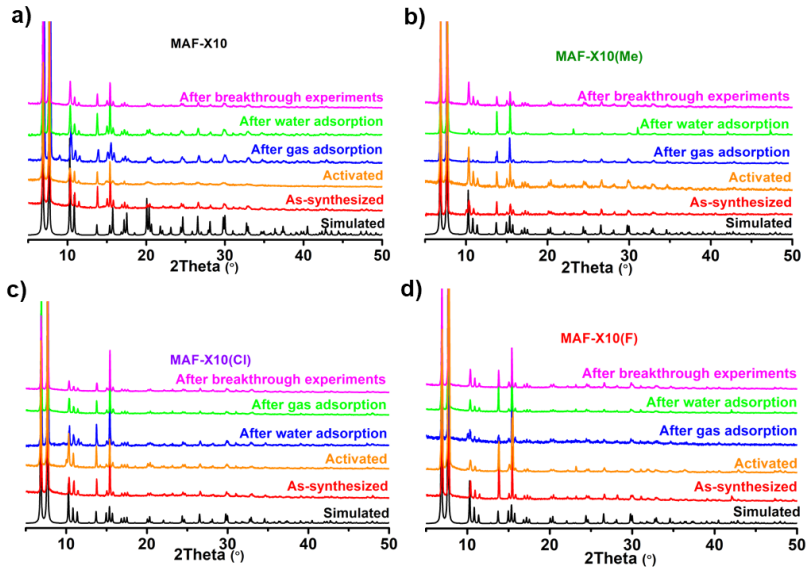

Figure S1. PXRD patterns of simulated from crystal structure, as-synthesized, activated, after water adsorption, gas adsorption, and breakthrough experiment samples for a) MAF-X10; b) MAF-X10(Me); c) MAF-X10(Cl); d) MAF-X10(F).

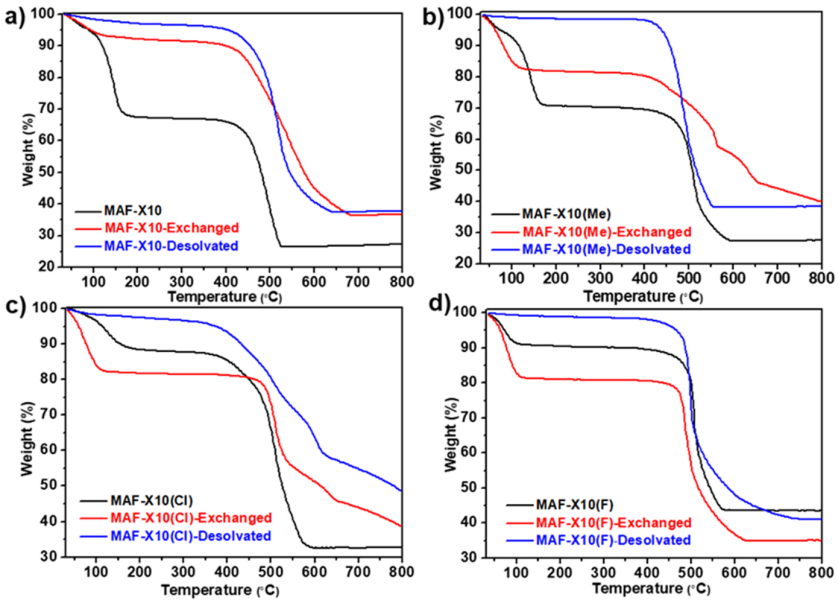

Figure S2. TGA curves of as-synthesized and dichloromethane-exchanged samples of a) MAF-X10; b) MAF-X10(Me); c) MAF-X10(Cl); d) MAF-X10(F).

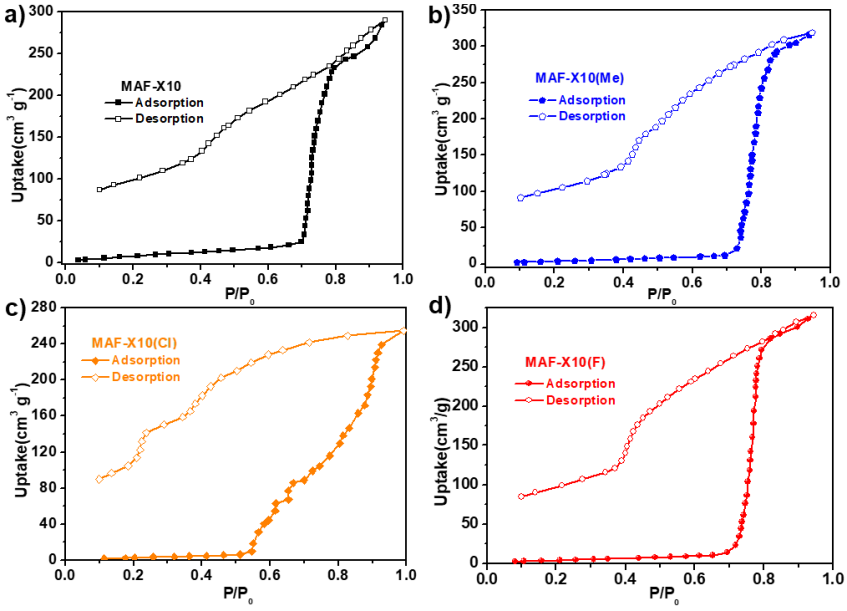

Figure S3. Water vapor adsorption and desorption isotherm of a) MAF-X10; b) MAF-X10(Me); c) MAF-X10(Cl); d) MAF-X10(F) at 298 K.

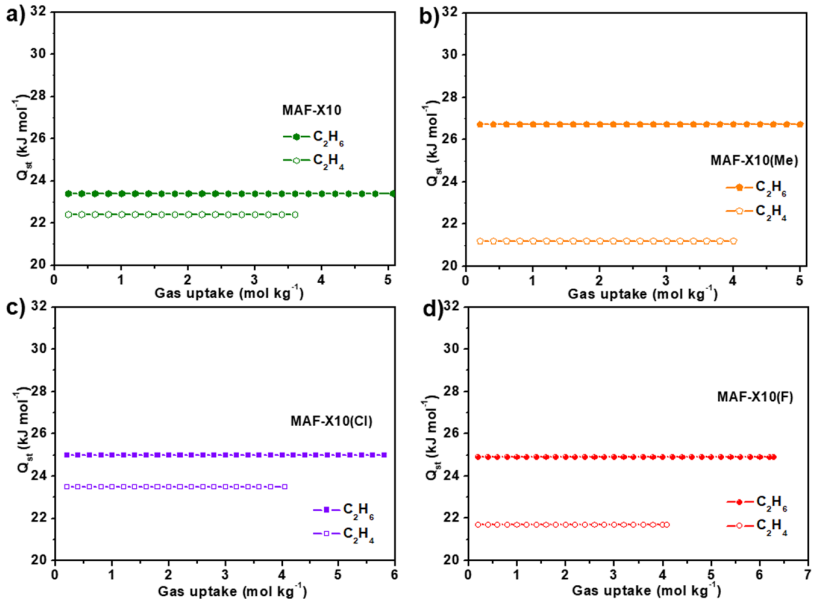

Figure S4.a) Adsorption enthalpies (Q_{st}) of C_2H_6 (solid) and C_2H_4 (hollow) for MAF-X10; b) adsorption enthalpies (Q_{st}) of C_2H_6 (solid) and C_2H_4 (hollow) for MAF-X10(Me); c) adsorption enthalpies (Q_{st}) of C_2H_6 (solid) and C_2H_4 (hollow) for MAF-X10(Cl); d) adsorption enthalpies (Q_{st}) of C_2H_6 (solid) and C_2H_4 (hollow) for MAF-X10(F).

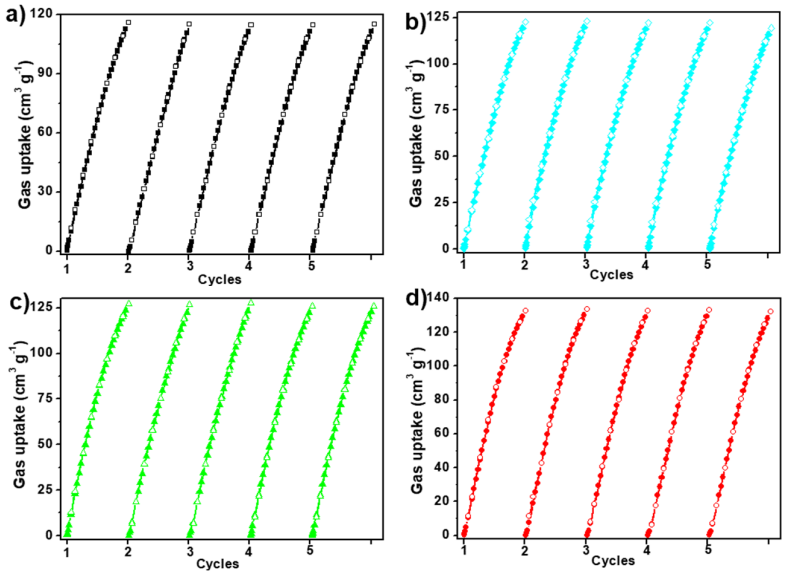

Figure S5. Cycles of C_2H_6 adsorption for a) MAF-X10; b) MAF-X10(Me), c) MAF-X10(Cl) and d) MAF-X10(F) at 298 K.

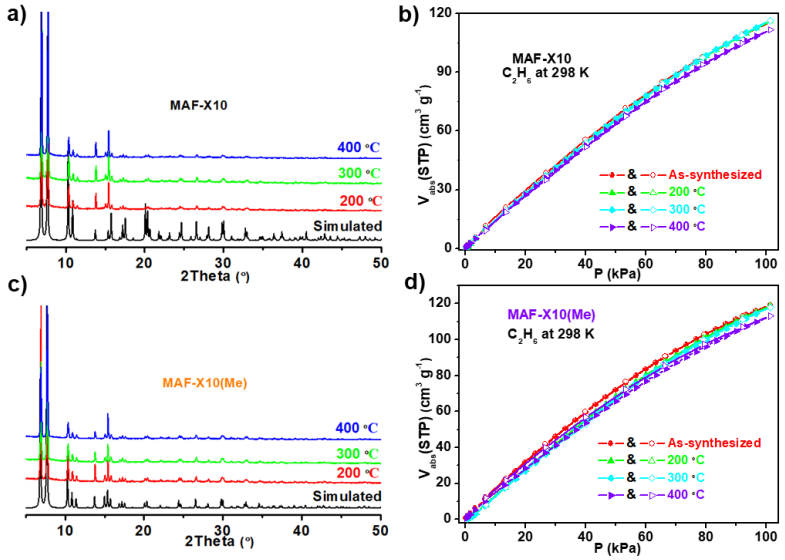

Figure S6. a) and b) PXRD patterns of MAF-X10 treated under different temperatures, C_2H_6 sorption isotherms at 298 K of MAF-X10 treated under different temperature; c) and d) PXRD patterns of MAF-X10(Me) treated under different temperatures, C_2H_6 sorption isotherms at 298 K of MAF-X10(Me) treated under different temperature.

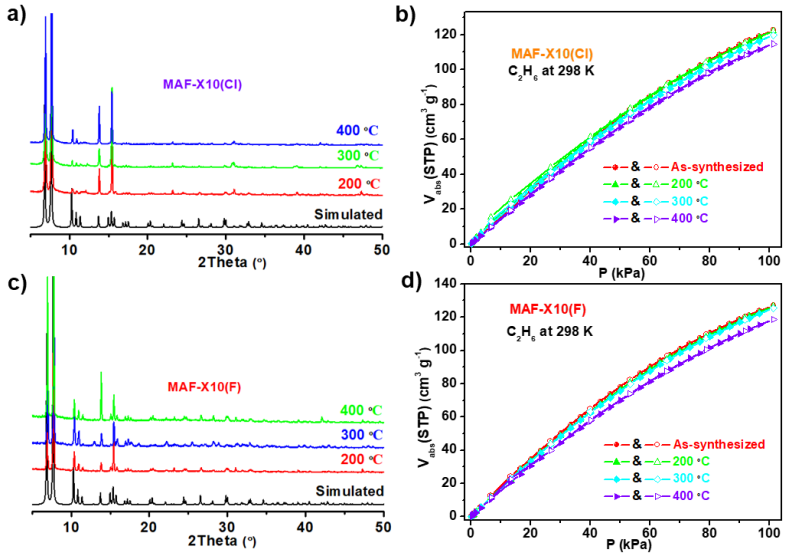

Figure S7. a) and b) PXRD patterns of MAF-X10(Cl) treated under different temperatures, C_2H_6 sorption isotherms at 298 K of MAF-X10(Cl) treated under different temperature; c) and d) PXRD patterns of MAF-X10(F) treated under different temperatures, C_2H_6 sorption isotherms at 298 K of MAF-X10(F) treated under different temperature.

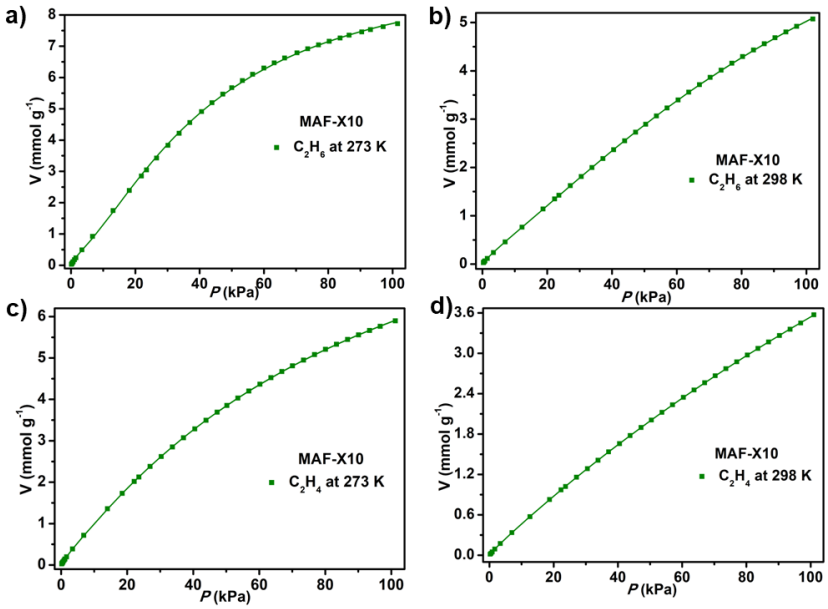

Figure S8. a) and b) C_2H_6 adsorption isotherms of MAF-X10 with fitted by dual L-F model at 273 K (a) and 298 K (b), 273 K: a1 = 9.40912, b1 = 0.00364, c1 = 1.50211, a2 = 0.33029, b2 = 0.79455, c2 = 1.44408, Chi^2 = 0.00101, R^2 = 0.99989; 298 K: a1 = 9.94983, b1 = 0.00145, c1 = 1.38093, a2 = 0.53361, b2 = 0.14091, c2 = 0.96028, Chi^2 = 0.00005, R^2 =

0.99998; c) and d) C_2H_4 adsorption isotherms of MAF-X10 with fitted by dual L-F model at 273 K (c) and 298 K (d), 273 K: a1 = 10.89243, b1 = 0.00672, c1 = 1.10867, a2 = 0.15068, b2 = 0.63238, c2 = 1.04784, Chi^2 = 0.00003, R^2 = 0.99999; 298 K: a1 = 16.09448, b1 = 0.00262, c1 = 1.01164, a2 = 0.06281, b2 = 0.32365, c2 = 0.86659, Chi^2 = 5.0292E-6, R^2 = 1.

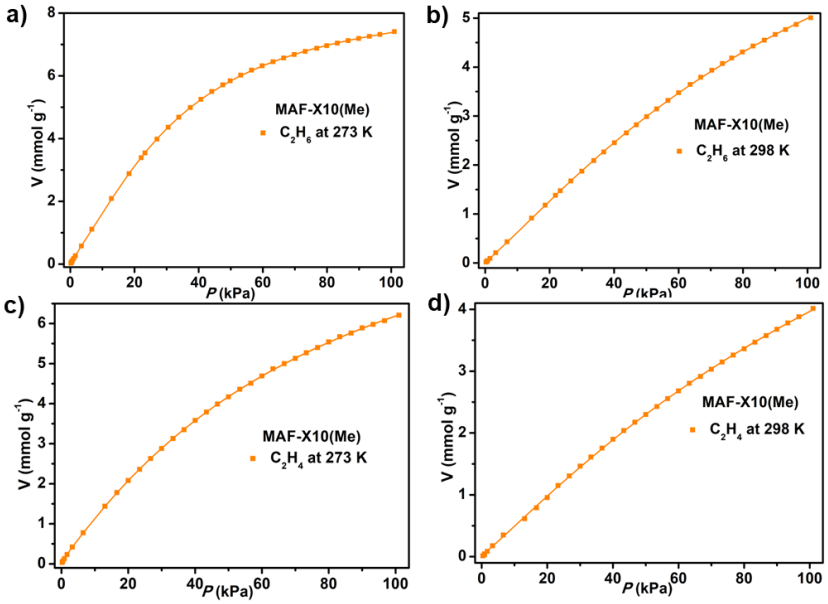

Figure S9. a) and b) C_2H_6 adsorption isotherms of MAF-X10(Me) with fitted by dual L-F model at 273 K (a) and 298 K (b), 273 K: a1 =8.16174, b1 = 0.00546, c1 = 1.49485, a2 = 0.51061, b2 = 0.33046, c2 = 1.23275, Chi^2 = 0.00012, R^2 = 0.99999; 298 K: a1 = 10.48867, b1 = 0.00351, c1 = 1.2003, a2 = 0.07733, b2 = 0.59516, c2 = 1.37423, Chi^2 = 0.0001, R^2 = 0.99997; c) and d) C_2H_4 adsorption isotherms of MAF-X10(Me) with fitted by dual L-F model at 273 K (c) and 298 K (d), 273 K: a1 = 10.8874, b1 = 0.00844, c1 = 1.08571, a2 = 0.13483, b2 = 0.78228, c2 = 1.08874, Chi^2 = 0.0001, R^2 = 0.99998; 298 K: a1 = 10.90779, b1 = 0.00351, c1 = 1.10354, a2 = 0.02684, b2 = 0.35294, c2 = 3.87813, Chi^2 = 0.00019, R^2 = 0.9999.

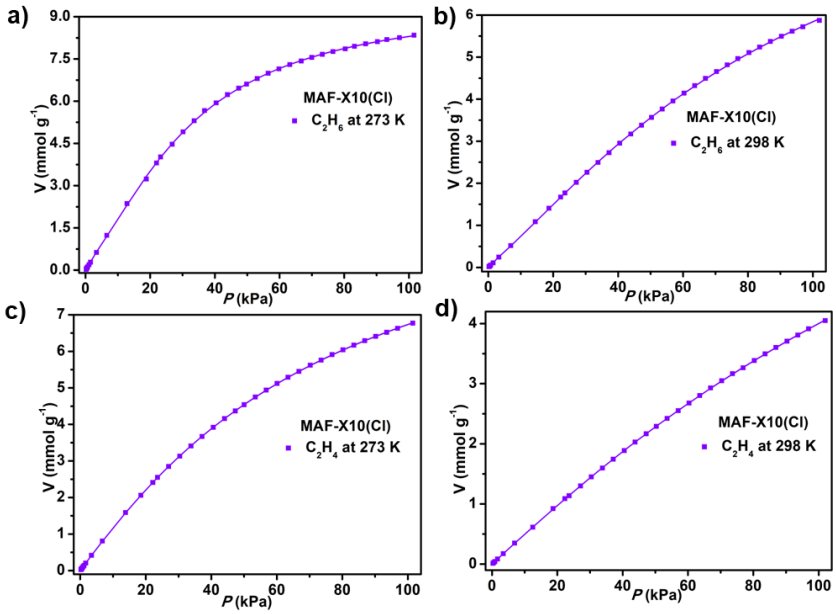

Figure S10. a) and b) C_2H_6 adsorption isotherms of MAF-X10(Cl) with fitted by dual L-F model at 273 K (a) and 298 K (b), 273 K: a1 = 8.85551, b1 = 0.00421, c1 = 1.58066, a2 = 0.69627, b2 = 0.2573, c2 = 1.32337, Chi^2 = 0.00067, R^2 = 0.99994; 298 K: a1 = 10.64733, b1 = 0.00307, c1 = 1.2865, a2 = 0.15369, b2 = 0.38806, c2 = 1.37816, Chi^2 = 0.00016, R^2 = 0.99996; c) and d) C_2H_4 adsorption isotherms of MAF-X10(Cl) with fitted by dual L-F model at 273 K (c) and 298 K (d), 273 K: a1 = 11.21304, b1 = 0.00742, c1 = 1.14242, a2 = 0.13783, b2 = 0.42681, c2 = 1.19246, Chi^2 = 0.00003, R^2 = 1; 298 K: a1 = 12.82673, b1 = 0.00316, c1 = 1.07547, a2 = 0.03242, b2 = 0.43114, c2 = 1.35749, Chi^2 = 0.00002, R^2 = 0.99999.

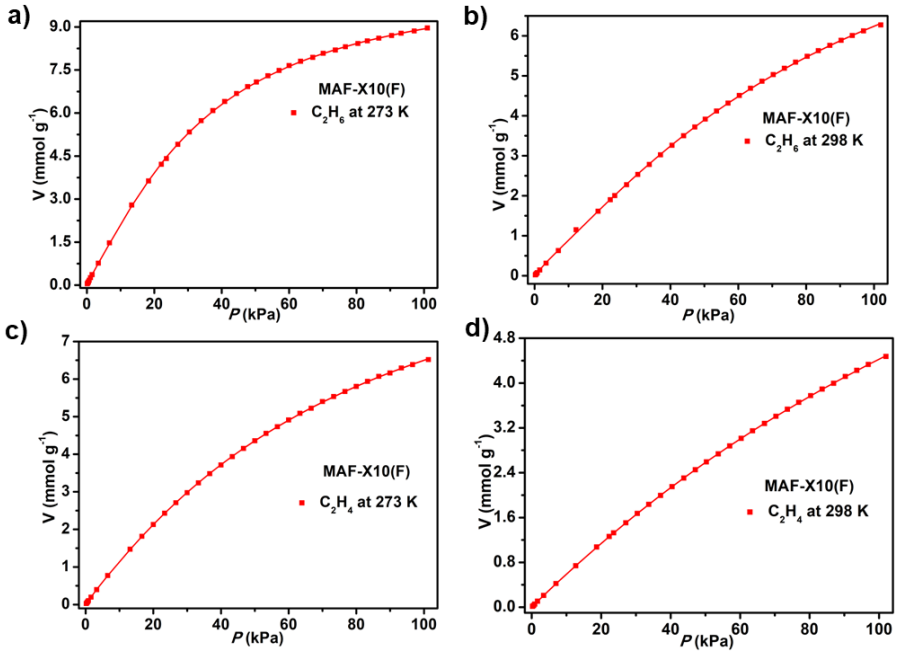

Figure S11. a) and b) C_2H_6 adsorption isotherms of MAF-X10(F) with fitted by dual L-F model at 273 K (a) and 298 K (b), 273 K: a1 = 10.3867, b1 = 0.00887, c1 = 1.35191, a2 = 0.44633, b2 = 0.51986, c2 = 1.10744, Chi^2 = 0.00037, R^2 = 0.99997; 298 K: a1 = 10.93585, b1 = 0.00336, c1 = 1.2755, a2 = 0.28759, b2 = 0.25276, c2 = 1.311, Chi^2 = 0.00035, R^2 = 0.99993; c) and d) C_2H_4 adsorption isotherms of MAF-X10(F) with fitted by dual L-F model at 273 K (c) and 298 K (d), 273 K: a1 = 11.25405, b1 = 0.00763, c1 = 1.11615, a2 = 0.1327, b2 = 0.43408, c2 = 1.28503, Chi^2 = 0.00009, R^2 = 0.99998; 298 K: a1 = 13.36461, b1 = 0.00347, c1 = 1.04621, a2 = 0.0503, b2 = 0.19085, c2 = 1.17644, Chi^2 = 2.8772E-6, R^2 = 1.

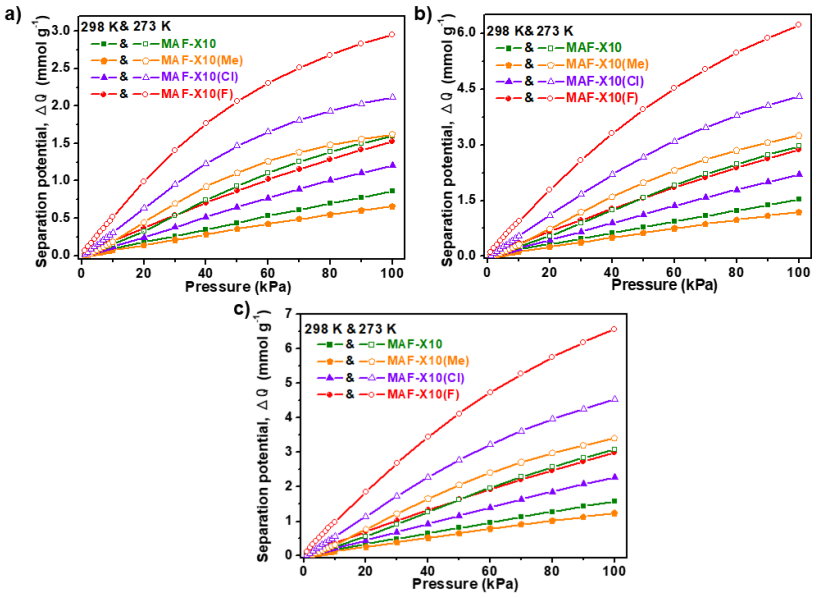

Figure S12. a-c) Separation potential of four MOFs for C_2H_6/C_2H_4 mixtures at 273 and 298 K: a) (v/v; 1/1), b) (v/v; 1/9), c) (v/v; 1/15) (solid curves represent 298 K and hollow curves represent 273 K; olive represent MAF-X10, orange represent MAF-X10(Me), violet represent MAF-X10(Cl) and red represent MAF-X10(F)).

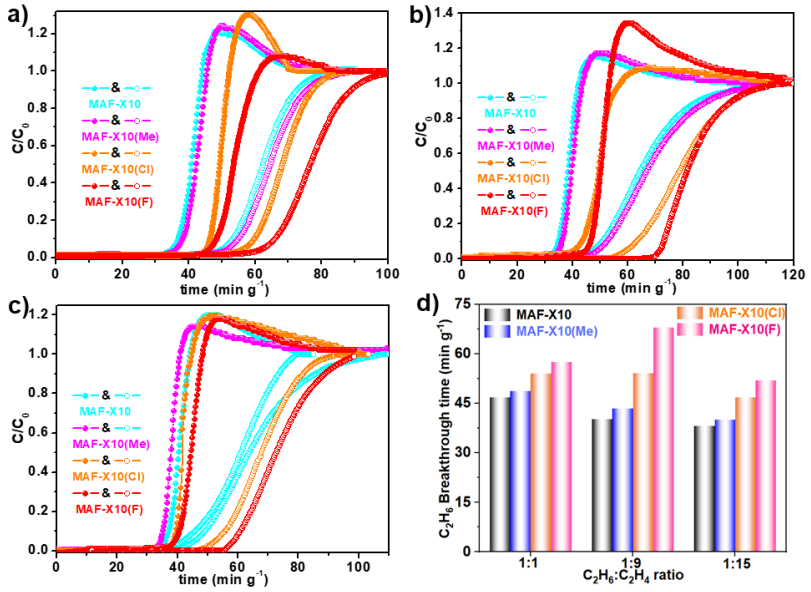

Figure S13. Experimental breakthrough curves for MAF-X10, MAF-X10(Me), MAF-X10(Cl) and MAF-X10(F) at 273 K and 100 kPa, a) (v/v; 5/5), b) (v/v; 1/9), c) (v/v; 1/15); d) C_2H_6 breakthrough time for MAF-X10, -(Me), -(Cl) and -(F) at 273 K.

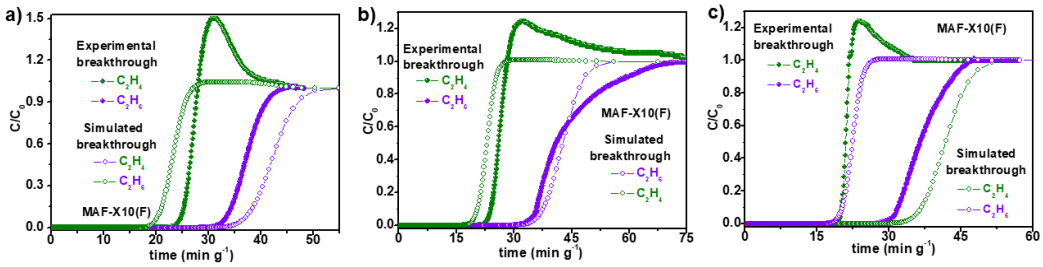

Figure S14. Comparison of the transient breakthrough curves and experimental breakthrough curves for MAF-X10(F) at 298 K: a) C_2H_6/C_2H_4 (5/5) mixtures, b) C_2H_6/C_2H_4 (1/9) mixtures, c) C_2H_6/C_2H_4 (1/15) mixtures.

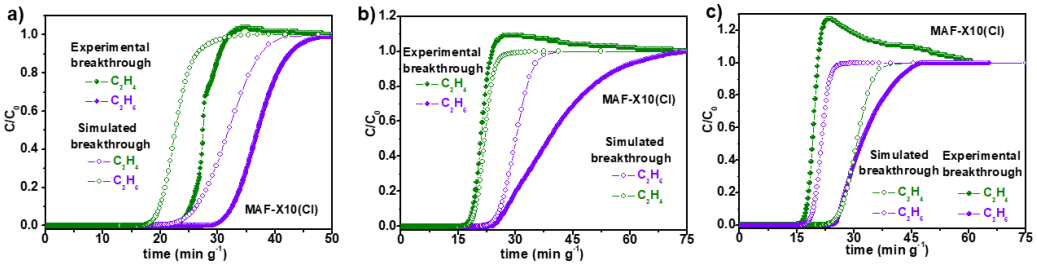

Figure S15. Comparison of the transient breakthrough curves and experimental breakthrough curves for MAF-X10(Cl) at 298 K: a) C_2H_6/C_2H_4 (5/5) mixtures, b) C_2H_6/C_2H_4 (1/9) mixtures, c) C_2H_6/C_2H_4 (1/15) mixtures.

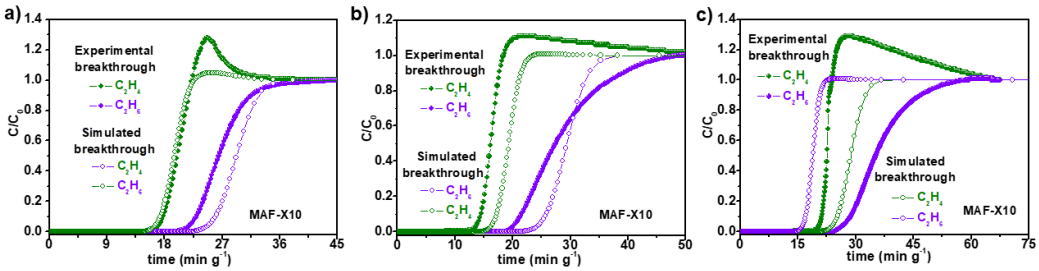

Figure S16. Comparison of the transient breakthrough curves and experimental breakthrough curves for MAF-X10 at 298 K: a) C_2H_6/C_2H_4 (5/5) mixtures, b) C_2H_6/C_2H_4 (1/9) mixtures, c) C_2H_6/C_2H_4 (1/15) mixtures.

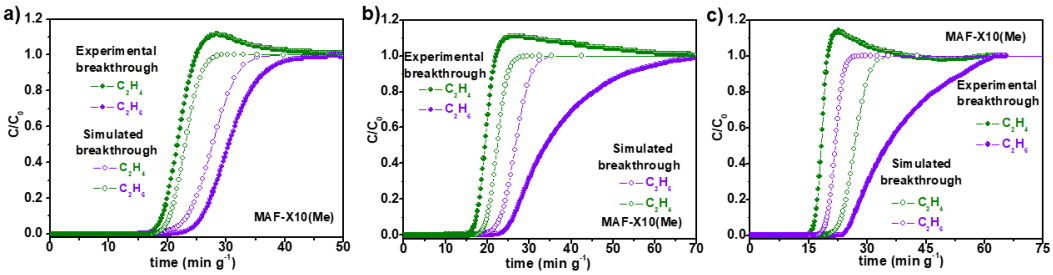

Figure S17. Comparison of the transient breakthrough curves and experimental breakthrough curves for MAF-X10(Me) at 298 K: a) C_2H_6/C_2H_4 (5/5) mixtures, b) C_2H_6/C_2H_4 (1/9) mixtures, c) C_2H_6/C_2H_4 (1/15) mixtures.

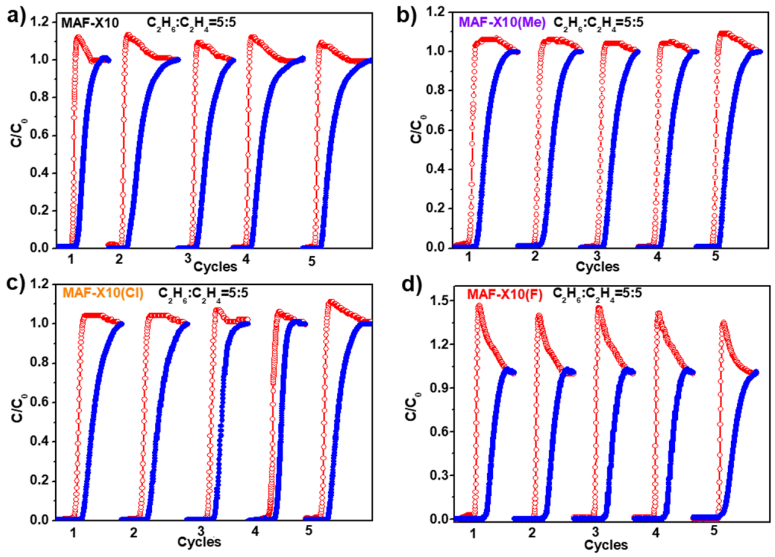

Figure S18. Cycling tests for equimolar C_2H_6/C_2H_4 (v/v; 5/5) mixtures at 298 K a) MAF-X10, b) MAF-X10(Me), c) MAF-X10(Cl), and d) MAF-X10(F).

Table S5. Crystal Data and Structure Refinements for MOFs.

	MAF-X10(Me)	MAF-X10(F)	MAF-X10(Cl)
Chemical formula	$C_{29}H_{30}N_8O_5Zn_4$	$C_{28}H_{27}FN_8O_5Zn_4$	$C_{28}H_{27}ClN_8O_5Zn_4$
Formula weight	832.09	836.05	852.50
T (K)	180(2) K	174(2) K	180(2) K
Crystal system	tetragonal	tetragonal	tetragonal
Space group	$P4_2/mcm$	$P4_2/mcm$	$P4_2/mcm$
a (Å)	11.5296(3)	11.5302(4)	11.5284(3)
b (Å)	11.5296(3)	11.5302(4)	11.5284(3)
c (Å)	25.8084(13)	25.768(2)	25.8176(13)
α (°), β (°), γ (°)	90,90,90	90,90,90	90,90,90
V (Å^3)	3430.8(2)	3425.7(4)	3431.3(2)
Z, $D_{calcd.}$[g·cm^{-3}]	2, 0.805	2, 0.811	2, 0.825
μ (mm^{-1}), Goof	1.406, 1.154	1.410, 1.179	1.444, 1.242
Reflns collected/unique/R_{int}	11324/1720/0.0473	11636/1701/0.07544	21768/1716/0.0438
Theta range for data collection	2.620 to 25.347°	2.620 to 25.366°	2.620 to 25.346°
R_1[a], wR_2[b] [I > 2σ]	0.0534, 0.1216	0.1144, 0.2575	0.0556, 0.1329
R_1[a], wR_2[b] (all data)	0.0580, 0.1235	0.1248, 0.2616	0.0583, 0.1341
CCDC number	2266974	2266975	2266976

[a]$R_1 = \Sigma(|F_o|-|F_c|)/\Sigma|F_o|$. [b]$R_2 = [\Sigma w(F_o^2 - F_c^2)^2/\Sigma w(F_o^2)^2]^{1/2}$.

Table S6. Selected bond lengths [Å] and angles [°] for MOFs.

MAF-X10(Me)					
Zn(1)-O(1)	1.9420(6)	O(1)-Zn(1)-O(2)	109.22(12)	O(1)-Zn(1)-N(1)	99.38(9)
Zn(1)-O(2)	1.961(4)	O(1)-Zn(1)-N(1)#1	99.38(9)	O(2)-Zn(1)-N(1)	112.32(10)
Zn(1)-N(1)#1	1.981(3)	O(2)-Zn(1)-N(1)#1	112.32(10)	N(1)#1-Zn(1)-N(1)	121.72(18)
Zn(1)-N(1)	1.981(3)				
MAF-X10(F)					
Zn(1)-O(2)	1.9418(15)	O(2)-Zn(1)-O(1)	108.9(3)	O(2)-Zn(1)-N(1)#1	99.96(19)
Zn(1)-O(1)	1.954(9)	O(2)-Zn(1)-N(1)	99.96(19)	O(1)-Zn(1)-N(1)#1	112.2(2)
Zn(1)-N(1)	1.978(7)	O(1)-Zn(1)-N(1)	112.2(2)	N(1)-Zn(1)-N(1)#1	121.3(4)
Zn(1)-N(1)#1	1.978(7)				
MAF-X10(F)					
Zn(1)-O(2)	1.9418(15)	O(2)-Zn(1)-O(1)	108.9(3)	O(2)-Zn(1)-N(1)#1	99.96(19)
Zn(1)-O(1)	1.954(9)	O(2)-Zn(1)-N(1)	99.96(19)	O(1)-Zn(1)-N(1)#1	112.2(2)
Zn(1)-N(1)	1.978(7)	O(1)-Zn(1)-N(1)	112.2(2)	N(1)-Zn(1)-N(1)#1	121.3(4)
Zn(1)-N(1)#1	1.978(7)				

Symmetry code: #1 = y, x, z.

Table S7. Adsorption data of MAF-X10 isomorphs and other representative materials.

Materials	C_2H_6 uptake ($cm^3\ g^{-1}$)	C_2H_6/C_2H_4 uptake ratio	Separation Potential (mmol g^{-1})	C_2H_6 Q_{st} (kJ mol^{-1})	reference
MAF-X10	113.6	1.42	0.856[a]		This work
MAF-X10(Me)	112.2	1.25	0.626[a]		
MAF-X10(Cl)	131.5	1.45	1.203[a]		
MAF-X10(F)	140.5	1.53	1.526[a]		
ZIF-8	56	1.75	0.313[a]	--	7
UPC-613	57.1	1.10	0.456[a]	31.8	8
UiO-67	48.8	1.43	0.465[a]	24.7	9
(Hf)DUT-52	90.0	1.25	1.284[a]	25.6	10
Tb-MOF-76(NH_2)	73.3	1.10	1.10[a]	32.8	11
Tb-MOF-76	68	1.09	0.727[a]	30.9	11
Ni(bdc)(ted)$_{0.5}$	112	1.47	1.132[a]	21	12
PCN-250	116.7	1.21	1.471[a]	23.6	13
MUF-15	105	1.30	1.256[a]	29.2	14
NKCOF-23	60.5	1.18	1.010[a]	24.3	15
CPOC-301	87	1.16	0.480[a]	32.4	16
CPM-733	159.6	1.10	0.850[a]	23.4	17
JNU-2	92	0.55	1.136[a]	29.4	18
MAF-49	38	1.02	1.361[a]	60	19
Fe(O_2)(dobdc)	74.3	1.37	1.739[a]	66.8	20
JNU-6-CH_3	103.7	1.18		24.7	21
HOF-NBDA	89.2	1.9	1.356[b]	23.8	22
Azole-Th-1	100.2	1.24	--	28.6	23

*a = C_2H_6/C_2H_4 (v/v, 50/50), b = C_2H_6/C_2H_4 (v/v, 10/90)

Table S8. Comparisons of C_2H_4 productivities of MAF-X10 isomorphs from the transient breakthrough simulations using C_2H_6/C_2H_4 mixtures as input.

MOFs	Gravimetric productivity (L Kg^{-1}) with different purities of C_2H_4		C_2H_4 Purity achieved
MAF-X10	C_2H_6/C_2H_4 (50/50,v/v)	5.945	99.96%
	C_2H_6/C_2H_4 (10/90,v/v)	17.685	99.95%
	C_2H_6/C_2H_4 (6.25/93.75,v/v)	19.628	99.96%
MAF-X10(Me)	C_2H_6/C_2H_4 (50/50,v/v)	2.938	99.51%
	C_2H_6/C_2H_4 (10/90,v/v)	4.278	99.95%
	C_2H_6/C_2H_4 (6.25/93.75,v/v)	6.663	99.95%
MAF-X10(Cl)	C_2H_6/C_2H_4 (50/50,v/v)	10.278	99.96%
	C_2H_6/C_2H_4 (10/90,v/v)	25.641	99.96%
	C_2H_6/C_2H_4 (6.25/93.75,v/v)	29.602	99.95%
MAF-X10(F)	C_2H_6/C_2H_4 (50/50,v/v)	22.044	99.95%

	C_2H_6/C_2H_4 (10/90,v/v)	43.965	99.95%
	C_2H_6/C_2H_4 (6.25/93.75,v/v)	47.874	99.95%

References

[1] R. Krishna, The Maxwell-Stefan Description of Mixture Diffusion in Nanoporous Crystalline Materials. Microporous Mesoporous Mater.185 (2014) 30-50.

[2] R. Krishna, Methodologies for Evaluation of Metal-Organic Frameworks in Separation Applications. RSC Adv. 5 (2019) 52269-52295.

[3] R. Krishna, Screening Metal-Organic Frameworks for Mixture Separations in Fixed-Bed Adsorbers using a Combined Selectivity/Capacity Metric. RSC Adv. 7 (2017) 35724-35737.

[4] R. Krishna, Methodologies for Screening and Selection of Crystalline Microporous Materials in Mixture Separations. Sep. Purif. Technol. 194 (2018) 281-300.

[5] R. Krishna, Metrics for Evaluation and Screening of Metal-Organic Frameworks for Applications in Mixture Separations. ACS Omega 5 (2020) 16987-17004.

[6] R. Krishna, Synergistic and Antisynergistic Intracrystalline Diffusional Influences on Mixture Separations in Fixed Bed Adsorbers. Precision Chemistry 1 (2023) 83-93.

[7] U. Böhme, B. Barth, C. Paula, A. Kuhnt, W. Schwieger, A. Mundstock, J. Caro and M. Hartmann, Ethene/Ethane and Propene/Propane Separation via the Olefin and Paraffin Selective Metal-Organic Framework Adsorbents CPO-27 and ZIF-8, Langmuir 29 (2013) 8592-8600.

[8] Y. Wang, C. Hao, W. Fan, M. Fu, X. Wang, Z. Wang, L. Zhu, Y. Li, X. Lu, F. Dai, Z. Kang, R. Wang, W. Guo, S. Hu, and D. Sun, One-step Ethylene Purification from an Acetylene/Ethylene/Ethane Ternary Mixture by Cyclopentadiene Cobalt-Functionalized Metal-Organic Frameworks, Angew. Chem. Int. Ed. 60 (2021) 11350-11358.

[9] X.-W. Gu, J.-X. Wang, E. Wu, H. Wu, W. Zhou, G. Qian, B. Chen, and B. Li, Immobilization of Lewis Basic Sites into a Stable Ethane-Selective MOF Enabling One-Step Separation of Ethylene from a Ternary Mixture, J. Am. Chem. Soc. 144 (2022) 2614-2623.

[10] X.-W. Gu, J. Pei, K. Shao, H.-M. Wen, B. Li, and G. Qian, Chemically Stable Hafnium-Based Metal-Organic Framework for Highly Efficient C_2H_6/C_2H_4 Separation under Humid Conditions, ACS Appl. Mater. Interfaces. 13 (2021) 18792-18799.

[11] G.-D. Wang, R. Krishna, Y.-Z. Li, W.-J. Shi, L. Hou, Y.-Y. Wang, and Z. Zhu, Boosting Ethane/Ethylene Separation by MOFs through the Amino-Functionalization of Pores, Angew. Chem. Int. Ed. 2022 (61) e202213015.

[12] W. Liang, F. Xu, X. Zhou, J. Xiao, Q. Xia, Y. Li, Z. Li, Ethane selective adsorbent $Ni(bdc)(ted)_{0.5}$ with high uptake and its significance in adsorption separation of ethane and ethylene, Chem. Eng. Sci. 148 (2016) 275-281.

[13] Y. Chen, Z. Qiao, H. Wu, D. Lv, R. Shi, Q. Xia, J. Zhou, Z. Li, An ethane-trapping MOF PCN-250 for highly selective adsorption of ethane over ethylene, Chem. Eng. Sci. 175 (2018) 110-117.

[14] O. T. Qazvini, R. Babarao, Z.-L. Shi, Y.-B. Zhang, and S. G. Telfer, A Robust Ethane-Trapping Metal-Organic Framework with a High Capacity for Ethylene Purification, J. Am. Chem. Soc. 2019, 141, 5014-5020.

[15] F. Jin, E. Lin, T. Wang, S. Geng, T. Wang, W. Liu, F. Xiong, Z. Wang, Y. Chen, P. Cheng, and Z. Zhang, Bottom-Up Synthesis of 8-Connected Three-Dimensional Covalent Organic Frameworks for Highly Efficient Ethylene/Ethane Separation, J. Am. Chem. Soc. 2022, 144, 5643-5652.

[16] K. Su, W. Wang, S. Du, C. Ji, D. Yuan, Efficient ethylene purification by a robust ethane-trapping porous organic cage, Nat Commun 12 (2021) 3703.

[17] H. Yang, Y. Wang, R. Krishna, X. Jia, Y. Wang, A. N. Hong, C. Dang, H. E. Castillo, X. Bu, and P. Feng, Pore-Space-Partition-Enabled Exceptional Ethane Uptake and Ethane-Selective Ethane-Ethylene Separation, J. Am. Chem. Soc. 142 (2020) 2222-2227.

[18] H. Zeng, X.-J. Xie, M. Xie, Y.-L. Huang, D. Luo, T. Wang, Y. Zhao, W. Lu, and D. Li, Cage-Interconnected Metal-Organic Framework with Tailored Apertures for Efficient C_2H_6/C_2H_4 Separation under Humid Conditions, J. Am. Chem. Soc. 141 (2019) 20390-20396.

[19] P.-Q. Liao, W.-X. Zhang, J.-P. Zhang and X.-M. Chen, Efficient purification of ethene by an ethane-trapping metal-organic framework, Nat. Commun. 6 (2015) 8697.

[20] L. Li, R.-B. Lin, R. Krishna, H. Li, S. Xiang, H. Wu, J. Li, W. Zhou, B. Chen, Ethane/ethylene separation in a metal-organic framework with iron-peroxo sites, Science 362 (2018) 443-446.

[21] X.-J. Xie, Y. Wang, Q.-Y. Cao, R. Krishna, H. Zeng, W. Lu and D. Li, Surface engineering on a microporous metal-organic framework to boost ethane/ethylene separation under humid conditions, Chem. Sci. 14 (2023) 11890-11895.

[22] Y. Zhou, C. Chen, R. Krishna, Z. Ji, D. Yuan, M. Wu, Tuning Pore Polarization to Boost Ethane/Ethylene Separation Performance in Hydrogen-Bonded Organic Frameworks, Angew. Chem. Int. Ed. 62 (2023) e202305041.

[23] Z. Xu, X. Xiong, J. Xiong, R. Krishna, L. Li, Y. Fan, F. Luo, B. Chen, A robust Th-azole framework for highly efficient purification of C_2H_4 from a $C_2H_4/C_2H_2/C_2H_6$ mixture, Nat. Commun. 11 (2020) 3163.